

Nano-FTIR Investigation of the CM Chondrite Allan Hills 83100

Jordan Young¹, Timothy D. Glotch¹, Mehmet Yesiltas², Victoria E. Hamilton³, Laura Brucia Breitenfeld¹, Hans A. Bechtel⁴, Stephanie Gilbert Corder⁵, and Ziheng Yao¹

¹Stony Brook University

²Kirklareli University

³Southwest Research Institute

⁴Advanced Light Source Division, Lawrence Berkeley National Laboratory

⁵Lawrence Berkeley National Laboratory

November 24, 2022

Abstract

Mid-infrared (MIR) spectroscopy has been used with great success to quantitatively determine the mineralogy of geologic samples. It has been employed in a variety of contexts from determining bulk composition of powdered samples to spectroscopic imaging of rock thin sections via micro-FTIR. Recent advances allow for IR measurements at the nanoscale. Near field nanoscale infrared imaging and spectroscopy with a broadband source (nano-FTIR) enable understanding of the spatial relationships between compositionally distinct materials within a sample. This will be of particular use when analyzing returned samples from Bennu and Ryugu, which are thought to be compositionally like CI or CM2 carbonaceous chondrites. Returned samples will likely contain olivine/pyroxene chondrules that have been transformed into hydrous phyllosilicates, sulfides, carbonates, and other alteration phases. The use of near-field infrared techniques to probe the boundaries between once pristine chondrules and alteration phases at the nanoscale is a novel approach to furthering our understanding of the compositional evolution of carbonaceous asteroids and the processes that drive their evolution. Here we report the results of nano-FTIR spectroscopy and imaging measurements performed on the carbonaceous chondrite Allan Hills (ALH) 83100 (CM1/2). We show with nanoscale resolution that spatially resolved Fe-Mg variations exist within the phyllosilicates around a chondrule rim. We also present effects of crystal orientation on the nano-FTIR spectra to account for the spectral differences between the meteorite and mineral spectra.

1 **Nano-FTIR Investigation of the CM Chondrite Allan Hills 83100**

2 **J. M. Young¹, T. D. Glotch¹, M. Yesiltas², V. E. Hamilton³, L. B. Breitenfeld¹, H. A. Bechtel⁴,**
3 **S. N. Gilbert Corder⁴, Z. Yao⁵**

4 ¹ Department of Geosciences, Stony Brook University, Stony Brook, NY, USA

5 ² Faculty of Aeronautics and Space Sciences, Kirklareli University, Kirklareli, Turkey

6 ³ Southwest Research Institute, Boulder, CO, USA

7 ⁴ Advanced Light Source, Lawrence Berkeley National Laboratory, Berkeley, CA, USA

8 ⁵ Department of Physics and Astronomy, Stony Brook University, Stony Brook, NY, USA

9

10 Corresponding author: Timothy D. Glotch (timothy.glotch@stonybrook.edu)

11 **Key Points:**

12 • Nano-FTIR spectroscopy provides extremely fine-scale (~20 nm) spatially resolved
13 mineralogic compositional information.

14 • Phyllosilicate spectra in ALH 83100 show Fe-Mg variations around a chondrule rim.

15 • Effects of crystallographic orientation on the nano-FTIR spectra are shown.

16

17 **Abstract**

18 Mid-infrared (MIR) spectroscopy has been used with great success to quantitatively determine the
19 mineralogy of geologic samples. It has been employed in a variety of contexts from determining
20 bulk composition of powdered samples to spectroscopic imaging of rock thin sections via micro-
21 FTIR. Recent advances allow for IR measurements at the nanoscale. Near field nanoscale infrared
22 imaging and spectroscopy with a broadband source (nano-FTIR) enable understanding of the
23 spatial relationships between compositionally distinct materials within a sample. This will be of
24 particular use when analyzing returned samples from Bennu and Ryugu, which are thought to be
25 compositionally like CI or CM2 carbonaceous chondrites. Returned samples will likely contain
26 olivine/pyroxene chondrules that have been transformed into hydrous phyllosilicates, sulfides,
27 carbonates, and other alteration phases. The use of near-field infrared techniques to probe the
28 boundaries between once pristine chondrules and alteration phases at the nanoscale is a novel
29 approach to furthering our understanding of the compositional evolution of carbonaceous asteroids
30 and the processes that drive their evolution. Here we report the results of nano-FTIR spectroscopy
31 and imaging measurements performed on the carbonaceous chondrite Allan Hills (ALH) 83100
32 (CM1/2). We show with nanoscale resolution that spatially resolved Fe-Mg variations exist within
33 the phyllosilicates around a chondrule rim. We also present effects of crystal orientation on the
34 nano-FTIR spectra to account for the spectral differences between the meteorite and mineral
35 spectra.

36

37 **Plain Language Summary**

38 NASA's OSIRIS-REx mission will return a sample of near-Earth asteroid Bennu to Earth in
39 September, 2023. Based on remote sensing analyses of the asteroid, it is expected that the sample
40 will be similar to CI or CM chondrite meteorites. Key remote sensing analyses of Bennu included
41 thermal infrared emission spectroscopy. In this work, we conduct infrared spectral analyses of
42 Allan Hills 83100, a CM 1/2 chondrite that shares spectral similarities to Bennu. We use
43 synchrotron near-field infrared (nano-IR) measurements to analyze the sample at scales of about
44 30 nm/pixel. This allows us to capture the spectra of very fine-grained components in meteorites
45 that contribute to their overall bulk spectra measured from remote sensing platforms. We document
46 the chemical alteration of a chondrule and show strong alteration gradients in the sample over
47 length scales smaller than 10 microns.

48 **1 Introduction**

49 Mid-infrared (MIR) spectroscopy has been used to great success towards quantitatively
50 determining the mineralogy of geologic samples (Hunt and Salisbury, 1970; Hapke, 1981;
51 Johnson, 1983; Clark and Roush, 1984; King and Ridley, 1987; Mustard and Pieters, 1987). It has
52 been employed in a variety of contexts from determining bulk composition of powdered samples
53 (Lane et al., 2011; Friedlander et al., 2015; Shirley and Glotch, 2019) to spectroscopic imaging of

54 rock sections via micro-Fourier transform infrared (micro-FTIR) (Yesiltas and Kebukawa, 2016;
55 Jaret et al., 2015, 2018; Farrand et al., 2016, 2018; Yesiltas et al. 2019; Johnson et al., 2020).

56 The spatial resolution of MIR spectroscopic measurements has typically been limited by
57 the diffraction limit of light, resulting in minimum spot sizes of $\sim 1 \mu\text{m}$ at synchrotron facilities
58 with bright infrared light sources (Nasse et al. 2011; Yesiltas et al. 2017). In their seminal paper,
59 Amarie et al. (2009) demonstrated the first continuous infrared spectroscopic measurements at
60 nanoscale ($\sim 20 \text{ nm}$) resolution, achieved by coupling an FTIR spectrometer with a scanning near
61 field optical microscope (SNOM), the latter of which had already demonstrated nm resolution in
62 the visible wavelength range (Dürig et al., 1986).

63 The advent of near-field infrared (nano-FTIR) spectroscopy and imaging has allowed for
64 measurement of the vibrational spectra of material monolayers and even single molecule
65 complexes (Xu et al., 2012; Amenabar et al., 2013). The ability to make high signal-to-noise ratio
66 (SNR) measurements at high spatial resolutions makes the nano-FTIR technique an excellent
67 method of analysis when sample availability is low or scientific questions to be addressed require
68 high spatial resolution. This makes nano-FTIR an extremely effective tool for the study of
69 extraterrestrial planetary materials. Dominguez et al. (2014) used nano-FTIR to study the
70 chemistry of a single cometary dust grain from Comet 81P/Wild 2, collected during NASA's
71 Stardust mission. Others have used nano-FTIR to study understand nano-scale mineral and organic
72 compositional variation in carbonaceous and ordinary chondrites, resulting from various parent
73 body alteration processes (Kebukawa et al., 2019; Glotch et al., 2019; Yesiltas et al., 2020, 2021).

74 The nano-FTIR method, and the previous works that have employed its use, will be of
75 particular use when analyzing returned samples of the near-Earth asteroids Bennu and Ryugu from
76 the OSIRIS-REx and Hayabusa-2 missions respectively. Both of these C-type asteroids are thought

77 to be compositionally analogous to the CI or CM2 carbonaceous chondrites (King et al., 2015;
78 Kitazato et al., 2019), which have undergone varying degrees of aqueous alteration. Recent results
79 have confirmed hydrated and volatile-rich bulk composition of Bennu as well as the linkage
80 between Bennu and carbonaceous chondrites (Lauretta et al., 2019). Returned samples will likely
81 contain organics, phyllosilicates, carbonates, and other alteration phases (Hamilton et al., 2019,
82 2021; Kaplan et al., 2020; Breitenfeld et al., 2021). The use of near-field infrared techniques to
83 probe the boundaries between once pristine chondrules and alteration phases at the nanoscale is a
84 novel approach to further improving our understanding of the compositional evolution of
85 carbonaceous asteroids and the processes that drive their evolution.

86 Furthermore, the use of nano-FTIR imaging and spectroscopy is an excellent tool for
87 understanding organic molecules found within carbonaceous chondrites and asteroid samples,
88 including the identity of those compounds and the spatial relationships between organic
89 compounds and mineralogical phases (Takir et al., 2013; Yesiltas et al., 2013, 2021). This
90 information may prove critical to understanding how complex organic compounds found in
91 meteorites and asteroid samples formed (Pearson et al., 2002; Simon et al., 2020). To that end,
92 here, we report the results of nano-FTIR spectroscopy and imaging measurements performed on
93 the carbonaceous chondrite ALH 83100 (CM1/2), a potential compositional analog for the asteroid
94 Bennu.

95 **2 Materials and Methods**

96 **2.1 Petrographic Imaging**

97 A reflected light mosaic of the ALH 83100 thin-section sample was formed by ‘stitching’
98 together individual microscopy images using the software PtGUI. Individual images used to create

99 mosaics were captured using a Fein Optic microscope with a 4x objective lens and an AM-Scope
100 MU1403 camera attachment.

101 2.2. Micro-FTIR Hyperspectral Imaging

102 We collected a hyperspectral micro-FTIR reflectance map of ALH 83100 using a Nicolet
103 iN10MX imaging spectrometer in the Center for Planetary Exploration at Stony Brook University.
104 The instrument is equipped with a 16-pixel MCT linear array detector operating in pushbroom
105 mode to acquire hyperspectral images over the $\sim 4000\text{--}500\text{ cm}^{-1}$ ($2.5\text{--}20\text{ }\mu\text{m}$) range. The micro-
106 FTIR image has a spatial resolution of $25\text{ }\mu\text{m}$ per pixel and a spectral resolution of 4 cm^{-1} . We
107 measured a sample-free region of a gold standard for calibration of the collected micro-FTIR data.
108 To display compositional variation across the sample, we utilized spectral indices (wavenumbers,
109 spectral channels, and band depths) to map the band strengths of the $3\text{ }\mu\text{m}$ OH/H₂O feature, the
110 $\sim 2.7\text{ }\mu\text{m}$ OH feature, and the $\sim 7\text{ }\mu\text{m}$ CO₃ feature. The most widely used and simplest method to
111 parameterize the presence and strength of spectral bands is a band depth index (e.g., Clark and
112 Roush, 1984; Viviano-Beck et al., 2014). The band strength (B) is calculated as the ratio of the
113 peak center maximum, C , at frequency ν_C , to C^* , the phase value on the continuum between points
114 L and H , located at frequencies ν_L and ν_H , respectively. Mathematically, $B = \mathbf{1} - \frac{C}{C^*} = \frac{aL+bH}{C}$
115 where $\mathbf{a} = \mathbf{1} - \mathbf{b}$ and $\mathbf{b} = \frac{\nu_C - \nu_L}{\nu_H - \nu_L}$. In practice, to increase index consistency in a spectrum that may
116 contain noise, the values of C , C^* , L , H , ν_L , ν_C , and ν_H may be averages of 2 or more spectral
117 channels.

118 2.3 Nano-FTIR Spectroscopy

119 We acquired nano-FTIR measurements at the Synchrotron Infrared Nano Spectroscopy

120 (SINS) beamline at the Advanced Light Source (ALS) at Lawrence Berkeley National Laboratory
121 (LBNL) (Bechtel et al. 2020). We collected both near-field infrared images at discrete wavelengths
122 and point spectra of a polished thin-section ($\sim 30 \mu\text{m}$ thickness) of the CM2 chondrite Allan Hills
123 (ALH) 83100. Spectra were collected using a neaspec neaSNOM near field system coupled with
124 a conductive atomic force microscope (AFM) tip for focusing the synchrotron infrared beam
125 source (Amarie et al., 2009; Bechtel et al. 2020). Scattering-type near-field phase and amplitude
126 spectra referenced to a gold standard were collected at harmonics of the AFM tapping frequency.
127 Far-field contributions to the acquired signal are removed by demodulating the signal at higher
128 harmonics of the tapping frequency ($n \geq 2$) (Hillebrand & Keilmann, 2000; Labardi et al. 2000).
129 Second harmonic ($n = 2$) data are presented here as a good compromise between near-field signal
130 and background suppression. Demodulation of the initial signal produces both an amplitude and a
131 phase spectrum. These spectra are to first order analogous with the reflectance and absorbance
132 spectra of typical far-field FTIR measurement (Bechtel et al., 2020), respectively. As such, we will
133 make frequent comparisons between amplitude-reflectance and phase-absorbance in this work. It
134 should be noted that the strong electromagnetic interaction between the AFM tip and the sample
135 surface can distort the shapes and positions of the major vibrational features, sometimes making
136 direct comparisons difficult. The spatial resolution of point spectroscopy measurements is
137 controlled by the radius of curvature of the AFM tip, which is $< 20 \text{ nm}$. Collected spectra had ~ 8
138 cm^{-1} spectral sampling.

139 For imaging, we used the same neaspec instrument operating in pseudo-heterodyne
140 imaging mode with two tunable lasers centered $\sim 1666 \text{ cm}^{-1}$ and $\sim 1000 \text{ cm}^{-1}$ respectively. As water
141 has an absorption at $\sim 1600 \text{ cm}^{-1}$ (H-O-H bending), we used the 1666 cm^{-1} laser to examine the
142 spatial distributions of hydrated mineral phases within the sample. Measurements made with the

143 1666-cm⁻¹ laser were at the discrete 1675, 1623, and 1572 cm⁻¹ wavenumbers, while
144 measurements made with the 1000-cm⁻¹ laser were taken at the 1081, 1039, 983, and 944 cm⁻¹
145 wavenumbers. We chose the 10- μ m laser to understand spectral variations regarding the prominent
146 10 μ m feature found in silicate minerals. Scanned image area dimensions were 11 μ m \times 11 μ m,
147 and collected images had dimensions of 550 pixels \times 550 pixels, yielding an image resolution of
148 20 nm/pixel. The integration time was 7 ms at each spot, yielding a collection time of ~35 minutes
149 per image. Like the point spectra, phase and amplitude spectral maps were collected at the tapping
150 frequency of the AFM tip.

151 2.4 Sample and Sampling Location

152 ALH 83100 is a type 1/2 CM Antarctic meteorite find with a weathering grade of Be,
153 meaning that the presence of moderate rusting and evaporate minerals caused by terrestrial
154 weathering are observed on this sample. It is slightly more hydrated than conventional CM2
155 chondrites (Zolensky et al. 1997), hence the classification of CM1/2. ALH 83100 is composed of
156 ~85 % hydrous phyllosilicates and contains minor abundances (< 3 wt. %) of magnetite, sulfates,
157 and calcite respectively (Howard et al., 2011; Hanna et al., 2019). It has been extensively altered
158 by aqueous activity (De Leuw et al., 2009). 1.9 wt.% C was identified in ALH 83100 by Alexander
159 et al. (2013). It is composed of ~ 0.76 wt. % insoluble organic material (IOM), in which several
160 amino acids have been detected (Alexander et al., 2007; Elsila et al., 2012). Another 8-9 wt. % of
161 ALH 83100 is made up of the primary ferromagnesian silicate phases olivine and pyroxene in the
162 form of chondrule grains and chondrule fragments. Its carbonate abundance is ~2.8 vol% (De
163 Leuw et al. 2010). For this work, a polished thin section (~30 μ m thickness) of ALH 83100 was
164 loaned from the US Antarctic Meteorite collection at Johnson Space Center (JSC). In this sample,
165 we chose to target the interface between one such chondrule and the surrounding fine-grained

166 matrix. This boundary zone was targeted because it might provide information regarding the
 167 aqueous alteration of the primary chondrule minerals into the hydrous phyllosilicate alteration
 168 products in the surrounding matrix.

169 The reflected light microscopy and micro-FTIR composite images of ALH 83100 are
 170 shown in Figure 1. The colors shown in the RGB image are representative of common features
 171 observed in the spectra of the hyperspectral map image: red represents a relatively strong C-H
 172 stretch absorption, green represents a CO₃ (carbonate) stretch reflectance feature, and blue
 173 represents a strong O-H stretch absorption feature. Spectra containing O-H stretch features likely
 174 represent serpentine minerals, which are hydroxylated phyllosilicates that are common in CM
 175 chondrites. These indicate aqueous alteration, making blue zones of particular interest. Based on
 176 the prominence of hydroxylated mineral signatures, we chose the chondrule indicated by the arrow
 177 in Figure 1a. This chondrule displays strong O-H stretch features and is also bordered by material
 178 that is both faintly red and blue in the hyperspectral image. This suggests that the outlying matrix

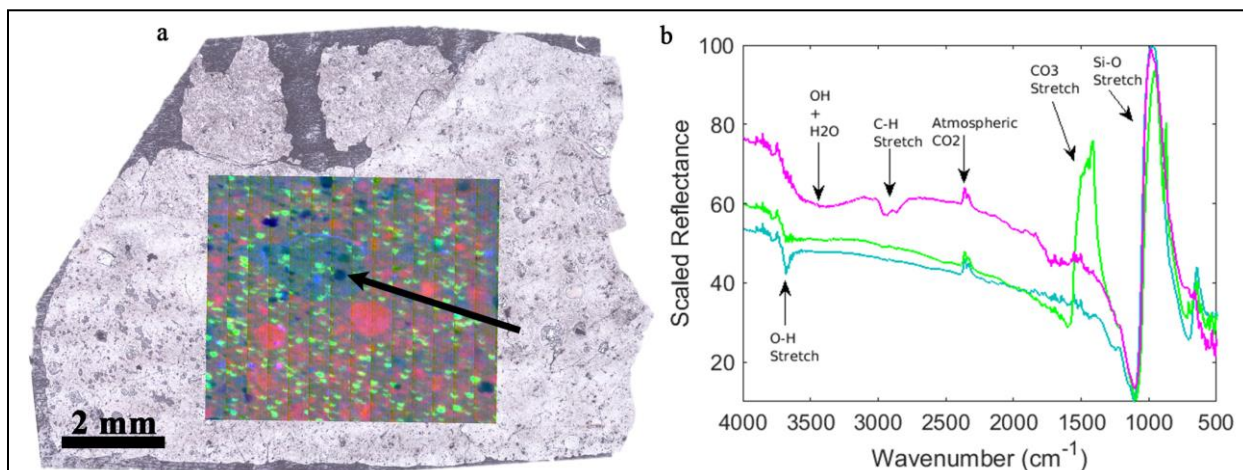


Figure 1. (a) RGB composite micro-FTIR map collected from ALH 83100 overlain on a corresponding reflected light microscopy image mosaic; Black arrow points at the chosen target chondrule shown as a dark blue circle. (b) Scaled micro-FTIR reflectance spectra containing the spectral features to which the RGB pixels of the micro-FTIR hyperspectral map are tied: The pink spectrum contains a strong C-H stretch feature (organic carbon), the green spectrum contains a strong CO₃ stretch feature (carbonate phases), and the blue spectrum contains a strong O-H stretch feature (hydrous minerals).

179 also contains hydrous minerals but also organic carbon. A closer inspection of the chondrule via
180 reflected light microscopy reveals that it is bisected by a large vein (Figure 2). Smaller veins are
181 seen throughout the chondrule. Rather than collect nano-FTIR measurements from these cracked
182 areas, we chose the ‘northern’ chondrule-matrix interface zone as the measurement area of interest
183 to maximize the compositional variability within the scene. The imaged region includes areas of
184 both chondrule and fine-grained matrix exposure compared to the slivers of matrix in the chondrule
185 interior. Our goal was to capture information regarding the spectral variability of these visibly

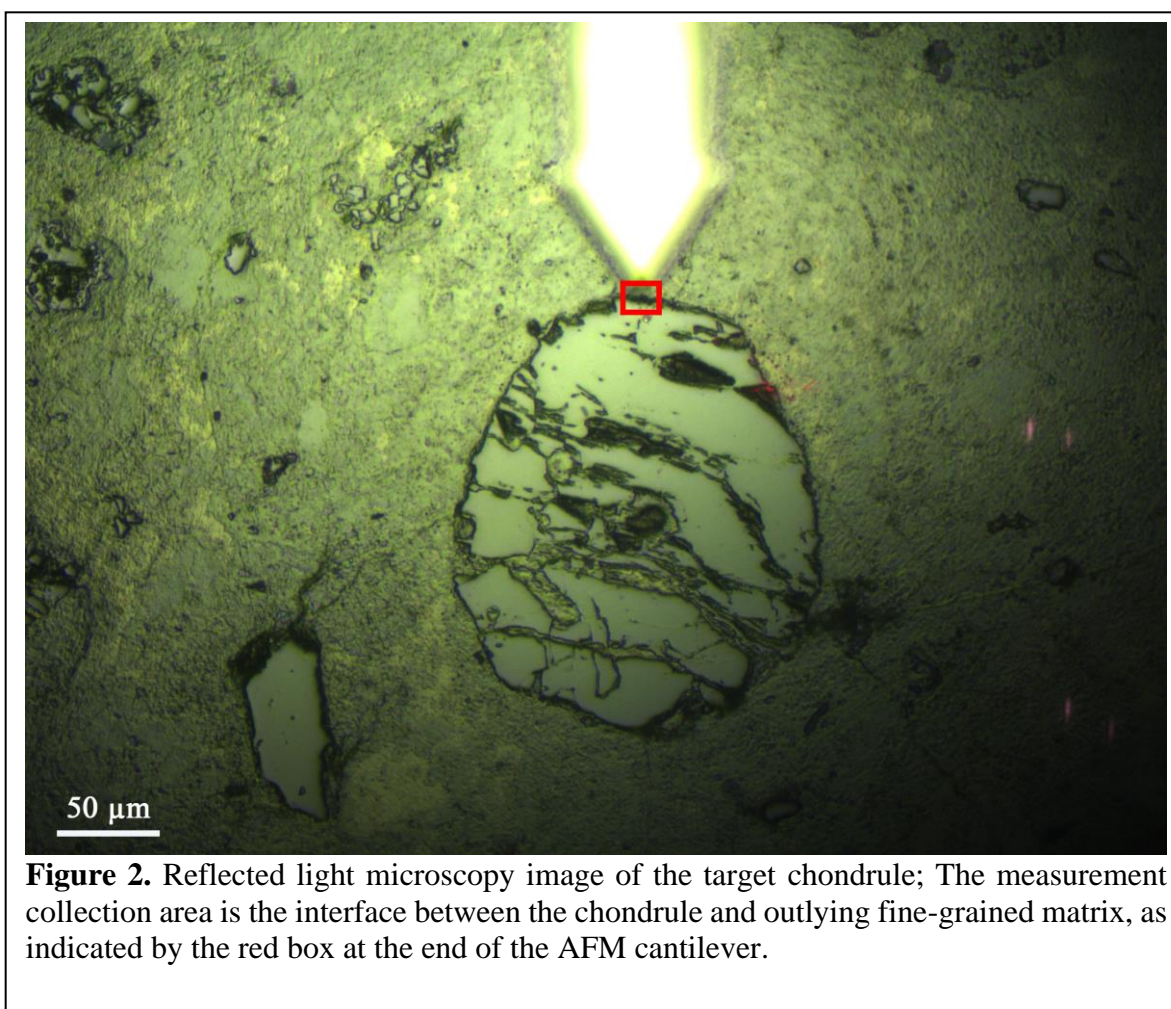
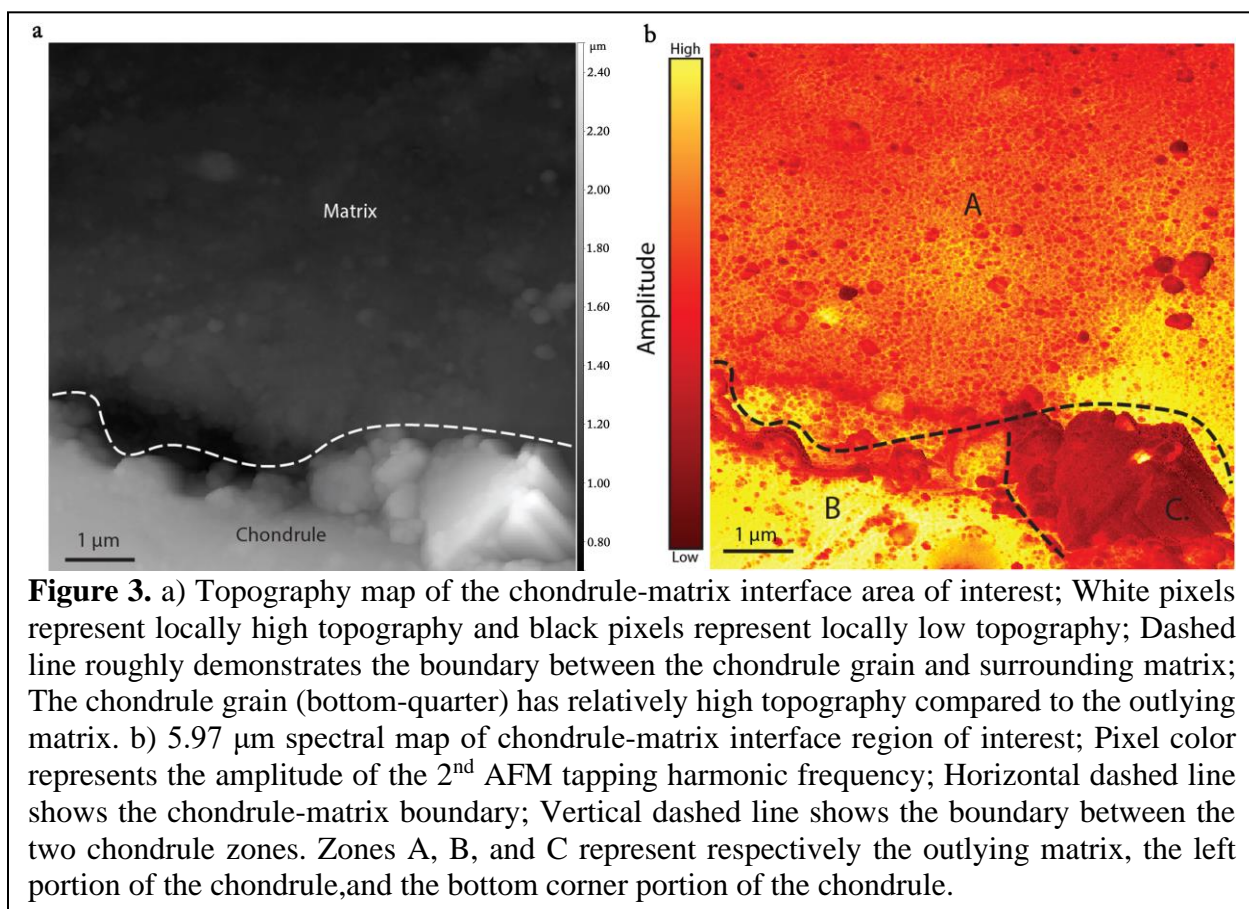


Figure 2. Reflected light microscopy image of the target chondrule; The measurement collection area is the interface between the chondrule and outlying fine-grained matrix, as indicated by the red box at the end of the AFM cantilever.

186 different types of materials as well differences between chondrule and matrix.

187 Nano-FTIR imaging allows simultaneous collection of sample topography with IR images.

188 The collected topographic map shows a high resolution view of the region of interest (Figure 3a)
 189 and clearly delineates the boundary zone of interest between the chondrule and the outlying matrix.
 190 The chondrule edge, in the bottom quarter of the map, has relatively high elevation compared to
 191 that of the outlying matrix, which makes up the majority of the scan. The low-lying matrix, shown



192 in shades of dark gray in Figure 3a, contains areas of higher topography. In general, there is some
 193 height difference ($< 1 \mu\text{m}$) between the chondrule grain and the fine-grained matrix area.

194 4. Results

195 We collected nano-FTIR images of the selected area of interest at wavelengths of 5.97,
 196 6.16, 6.36, 9.25, 9.621, 10.59, and 10.7 μm . All optical amplitude images shown here are 2nd
 197 harmonic optical amplitude images that are normalized within the individual image and are not on

198 a common scale. Beginning with the 5.97 μm map (Figure 3b.), striking compositional variability
199 is observed. The chondrule edge is divided into two section: the bottom left portion, which is
200 largely a high amplitude zone and the area in the right corner of the map, which has the lowest
201 amplitudes of the map. The 5.97 μm optical amplitude of the matrix also varies spatially. High
202 amplitude zones border the chondrule grain, while the top of the map is characterized by broadly
203 low amplitude zones. The area between these relatively homogenous regions of matrix is
204 characterized by the optical amplitude that varies at a spatial scale of $< 0.1 \mu\text{m}$. Features with radii
205 $< 0.5 \mu\text{m}$ are frequent in this region; these grains are generally low optical amplitude, but still vary.
206 Intra-chondrule variation exists at 6.16 and 6.36 μm as well (Figure 4.). The relationship between
207 the distinct zones of the exposed chondrule edge are maintained at these wavelengths: the left
208 portion has relatively higher optical amplitudes and the right portion has the lowest optical
209 amplitude pixels of the map. At both 6.16 and 6.36 μm , the left portion of the chondrule appears
210 less homogenous than at 5.97 μm . The left portion of the chondrule edge has relatively lower
211 optical amplitude at these wavelengths than at 5.97 μm . The edge of the chondrule at is better
212 defined at these wavelengths as well; the border is much lower optical amplitude than the
213 surrounding matrix at 6.16 and 6.36 than at 5.97. At 6.16 and 6.36 μm , the mottled or web like
214 amplitude variation seen in the matrix at 5.97 μm is even more prevalent. The spectral contrast
215 between the outlying grains and the fine-grained matrix, in which they are suspended, is also more
216 pronounced.

217

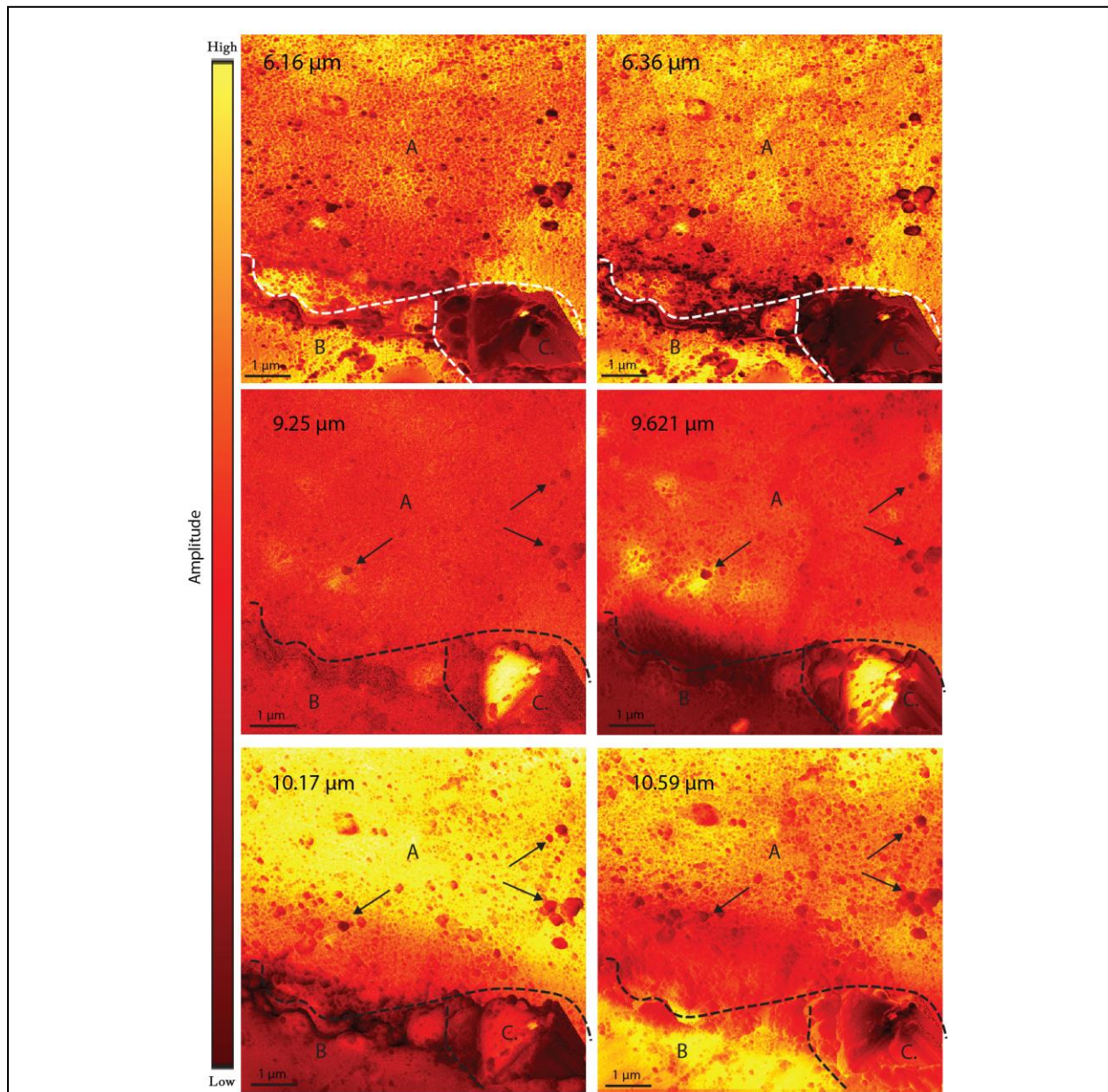
At 9.25 and 9.621 μm , intra-chondrule optical amplitude variation still exists (Figure 4.).

Figure 4. (top row) 6.16 and 6.36 μm spectral maps of chondrule-matrix interface region of interest; (middle row) 9.25 and 9.621 μm spectral maps of chondrule-matrix interface region of interest; (bottom row) 10.17 and 10.59 μm spectral maps; Horizontal dashed line shows the boundary chondrule-matrix boundary; Vertical dashed line shows the boundary between the two chondrule zones. Zones A, B, and C represent respectively the outlying matrix, the left portion of the chondrule, and the bottom corner portion of the chondrule. Pixel color represents the relative optical amplitude of the 2nd AFM tapping harmonic frequency; Black arrows indicate 'grains' suspended in the matrix with low optical amplitude values.

218 The left portion of the chondrule exposure is homogeneously low optical amplitude at both

219 wavelengths. In contrast, a part of the bottom right portion of the chondrule is very high optical
220 amplitude at both wavelengths. At 9.25 μm , the outlying fine-grained matrix is largely
221 homogenous with a low optical amplitude but does still exhibit weak nano-scale mottled variation.
222 Suspended grains (black arrows) also have low optical amplitude values at this wavelength. At
223 9.621 μm , the matrix is less homogenous with enclaves of high optical amplitude material and
224 more extensive nano-scale mottling. The small outlying grains are generally lower optical
225 amplitude than the surrounding matrix at 9.621 μm .

226 At 10.17 μm , intra-chondrule variation, observed at other wavelengths, has disappeared
227 (Figure 4). Instead, the whole chondrule exposure is characterized by low optical amplitude values.
228 At this wavelength, the fine-grained matrix can be described as two homogenous zones: (1) the
229 middling amplitude border zone (2) the high amplitude outer region. As the name implies, the
230 border portion of observed matrix, which immediately borders the chondrule and extends outward
231 for $\sim 1\text{-}2$ μm radially, has median amplitude values. These values increase as distance from the
232 chondrule grain increases. The outer region of matrix is homogeneously high optical amplitude
233 material at this wavelength. Observed variation in this region is caused by the low optical
234 amplitude of the small, suspended grains. At 10.59 μm , intra-chondrule variation returns, with the
235 left portion of the chondrule exposure displaying high optical amplitude values and the bottom
236 right zone having low optical amplitude pixels. There is also widespread variability within the
237 matrix at this wavelength. The matrix border region again has moderate optical amplitude values
238 and is relatively homogenous. Higher optical amplitude pixels and nanoscale amplitude mottling
239 characterize the outer matrix region. The matrix suspended grains all appear to have low optical
240 amplitude values at this wavelength.

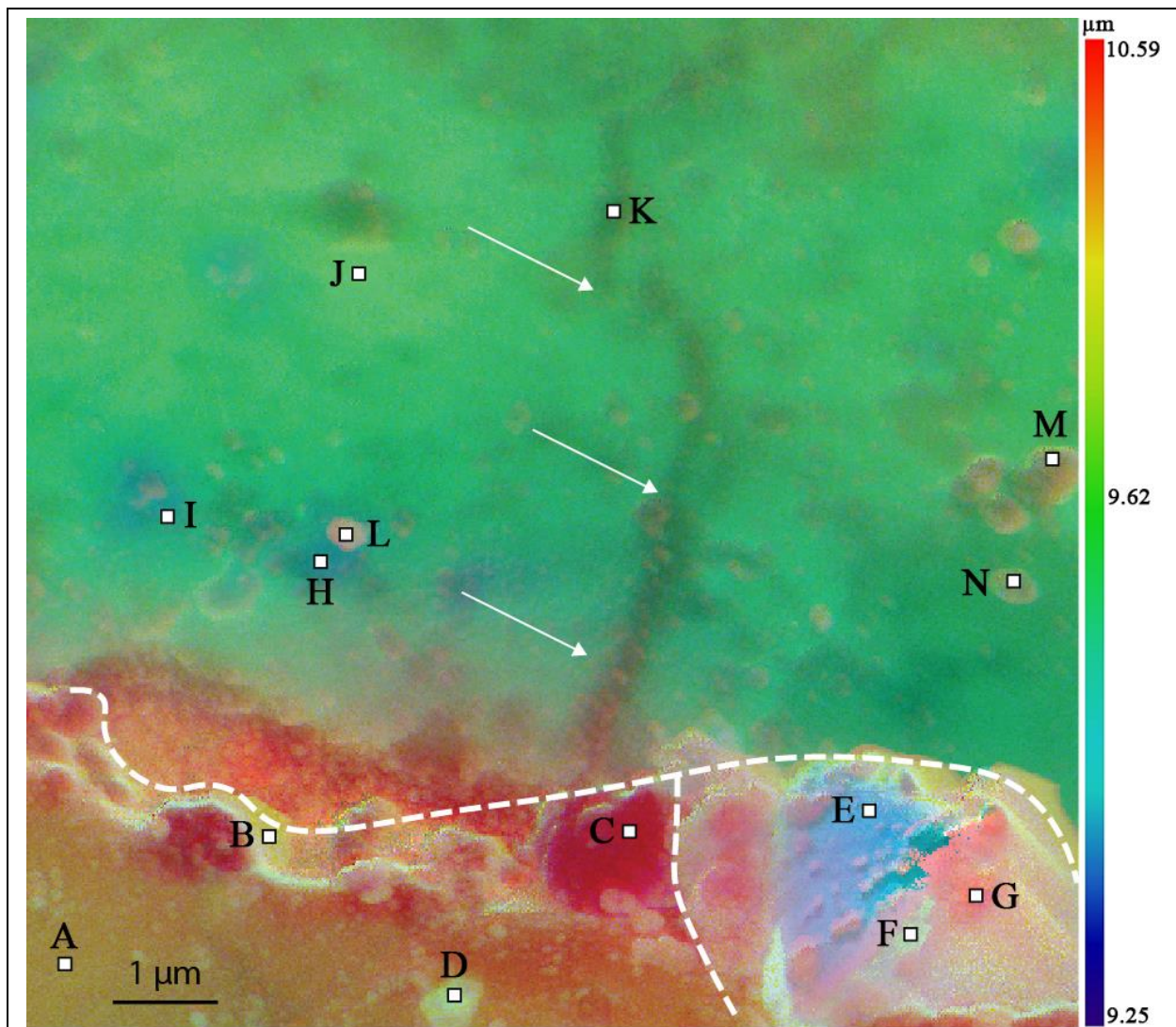


Figure 5. False color RGB image composite of the chondrule-matrix area of interest; R, G, and B color channels represent the 10.59, 9.62, and 9.25 μm wavelengths, respectively. Black edged squares represent positions where single spectra were collected. Arrows point to vein-like structure; Horizontal dashed line shows the chondrule-matrix border; Vertical dashed line shows border between chondrule zones; Points A, B, C, and D lie within the left chondrule zone; Points E, F, and G lie within the bottom right corner chondrule zone; Points H, I, J, K, L, M, and N lie within the matrix zone.

241 Using the map data collected at three discrete wavelengths, we generated a decorrelation
 242 stretched (DCS; Gillespie et al., 1986) false-color image that provides a clearer picture regarding
 243 the compositional variability in this portion of the sample. The color channels of the DCS map, R,
 244 G, and B represent the 10.59, 9.62, and 9.25 μm wavelengths, respectively. The exact data used to
 245 create the DCS maps, were individual 2nd harmonic phase maps for each wavelength, meaning that

246 the color of a pixel is tied to the phase value of its counterpart pixel from each relevant wavelength
 247 map. The DCS map (Figure 5) shows which areas of the map are spectrally similar and dissimilar,
 248 and corroborates observations of the individual wavelength maps. There is widespread spectral
 249 variability within the chondrule grain, within the matrix, and between the chondrule and matrix.
 250 The composite map displays the spectral contrast between the left portion of the chondrule
 251 exposure and the bottom right zone. In the composite map, the bottom left is shown in yellow and
 252 orange while the bottom right is mainly blue. The edge regions of the chondrule have coloring of
 253 pinks and red, distinguishing themselves from the more interior portions of the grain. The fine-
 254 grained matrix shown in Figure 5 is green, suggesting a maximum optical amplitude around 9.62
 255 μm , with minor variations in color and brightness. The observed small grains suspended in the
 256 fine-grained matrix vary in color, between orange, pink and blue, suggesting substantial spectral
 257 variability. Interestingly, this map also reveals a long vein like structure (white arrows), which had
 258 been obscured in the individual optical amplitude maps. This structure extends out radially from
 259 the chondrule exposure for $\sim 8 \mu\text{m}$ and has a width of $0.25\text{-}0.33 \mu\text{m}$.

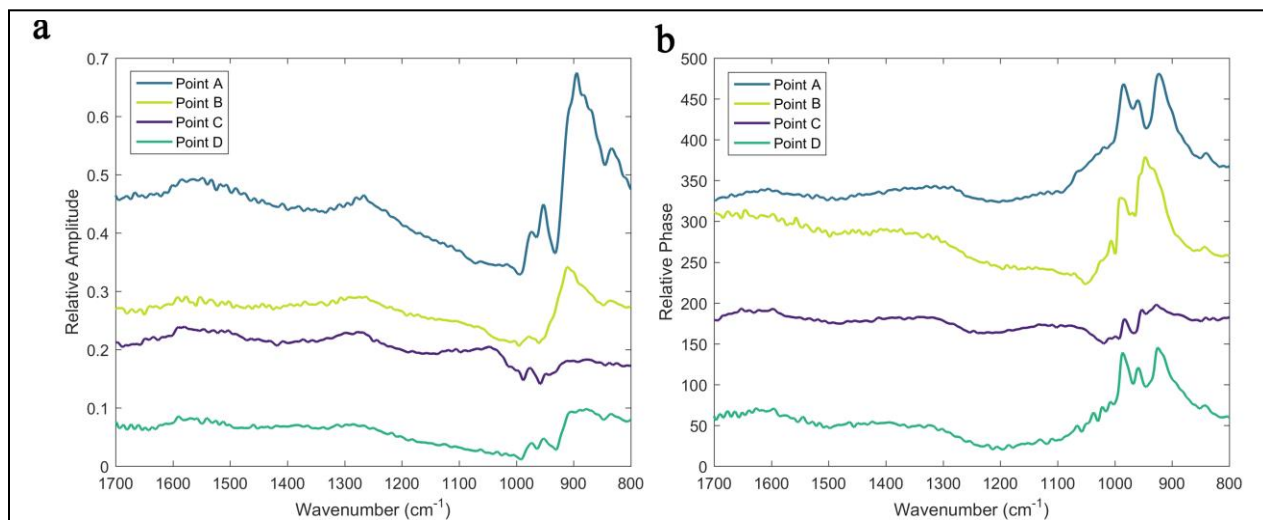


Figure 6. Nano-FTIR amplitude (a) and phase (b) spectra collected from the left portion of the chondrule exposure; Spectra have been stacked for comparison; amplitudes and phases are relative.

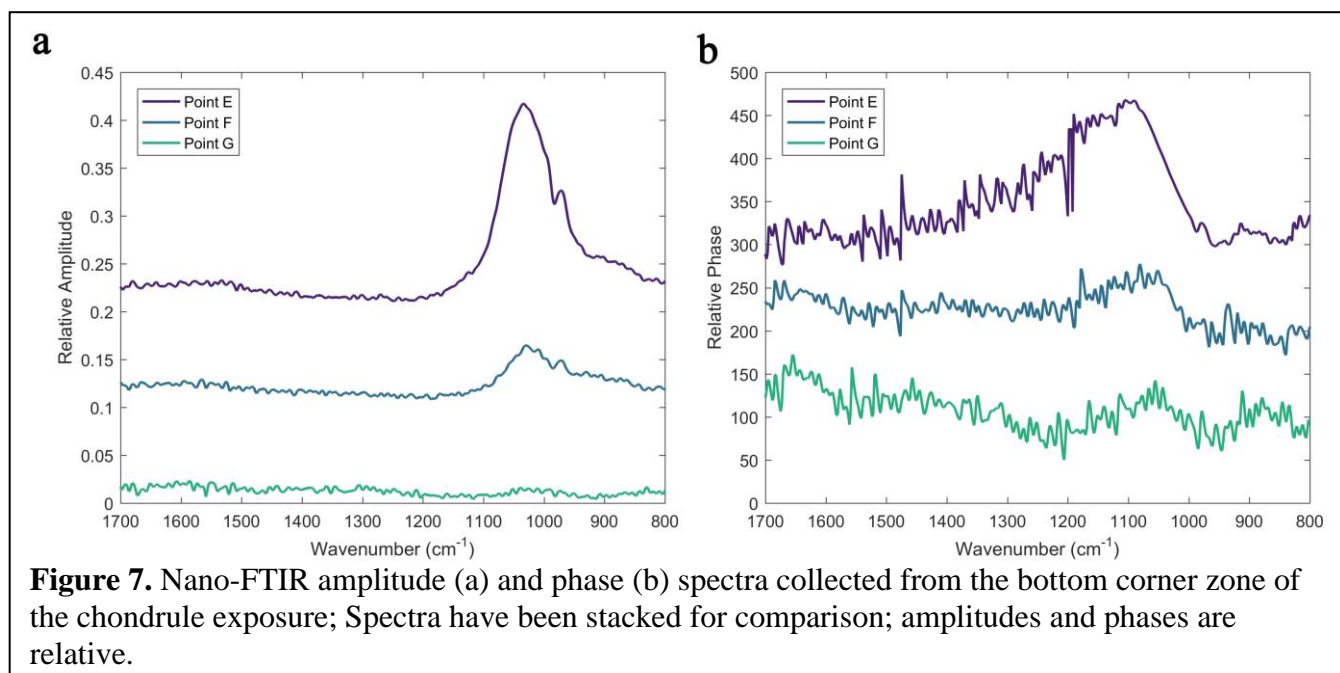
260 On the basis of spectral variability observed in the individual optical amplitude images and
261 the false color DCS map, we collected point spectra from various positions within the area of
262 interest. The positions from which the point spectra were collected can be seen in Figure 5. These
263 point spectra were collected from areas that belong to four categories: the left portion of the
264 chondrule exposure, the bottom right corner zone of the chondrule, the fine-grained matrix, and
265 the grains suspended in the matrix.

266 We collected spectra from four positions, A, B, C, and D, within the left portion of the
267 chondrule exposure (Figure 6). Amplitude spectrum C is relatively flat but has noticeable a broad
268 maximum centered at 1050 cm^{-1} . Spectrum A, by contrast, has a prominent amplitude maximum
269 at 890 cm^{-1} and several smaller features at 830 , 950 , and 970 cm^{-1} . Spectrum D also has a broad
270 amplitude maximum centered around 890 cm^{-1} , with additional features at 950 and 970 cm^{-1} .

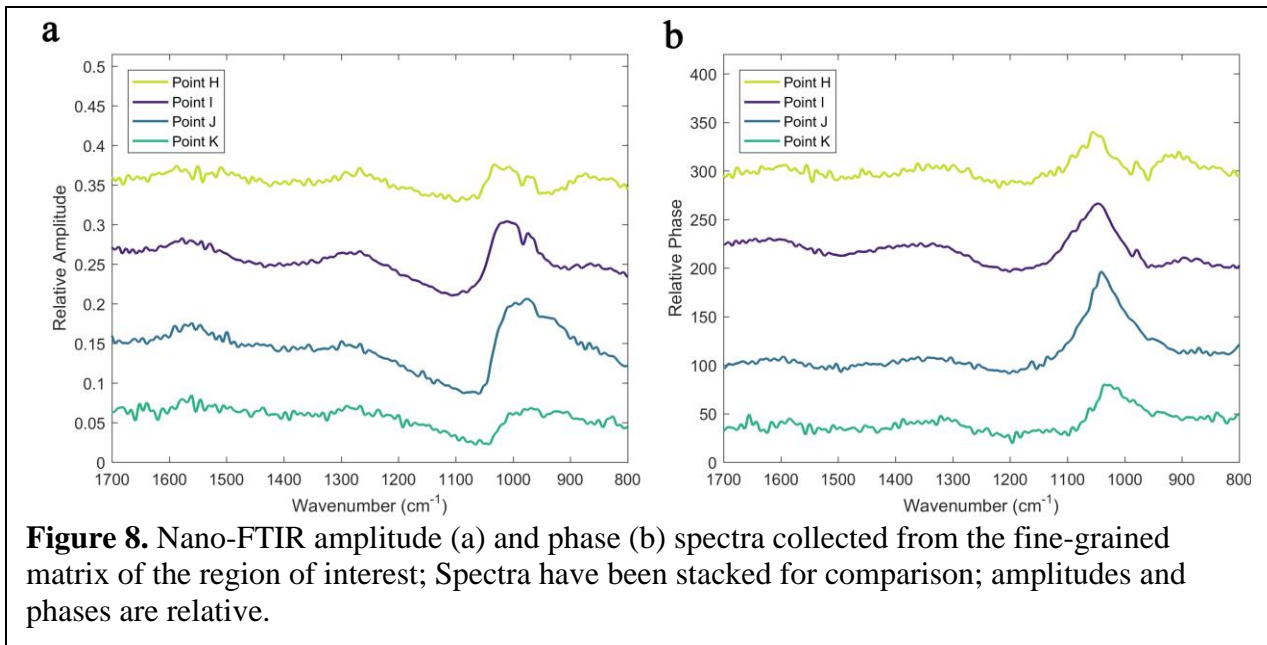
271 Phase spectra show that A and D have similar spectral profiles. They both have a triplet
272 with bands at 920 , 960 , 985 cm^{-1} . Spectrum B has a different profile. It presents prominent bands
273 at 950 and 990 cm^{-1} and a smaller feature at 1000 cm^{-1} . Similar to the amplitude spectrum, the
274 phase spectrum of C contains relatively weak features but bands at 927 , 953 and 985 cm^{-1} are still
275 visible.

276 From the bottom corner zone of the chondrule exposure, we collected spectra from three
277 positions: E, F, and G. The amplitude spectrum of point E (Figure 7.) shows one prominent
278 maximum centered at 1030 cm^{-1} and an ancillary feature at 970 cm^{-1} . Spectrum F has amplitude at
279 the same positions as spectrum E, but with lower amplitudes. The amplitude spectrum of point G
280 has less intense features. Their corresponding phase spectra are noiser. Spectrum E has a broad
281 peak with maxima at 1100 cm^{-1} and extends up to 1400 cm^{-1} . Spectra F and G have a maxima at

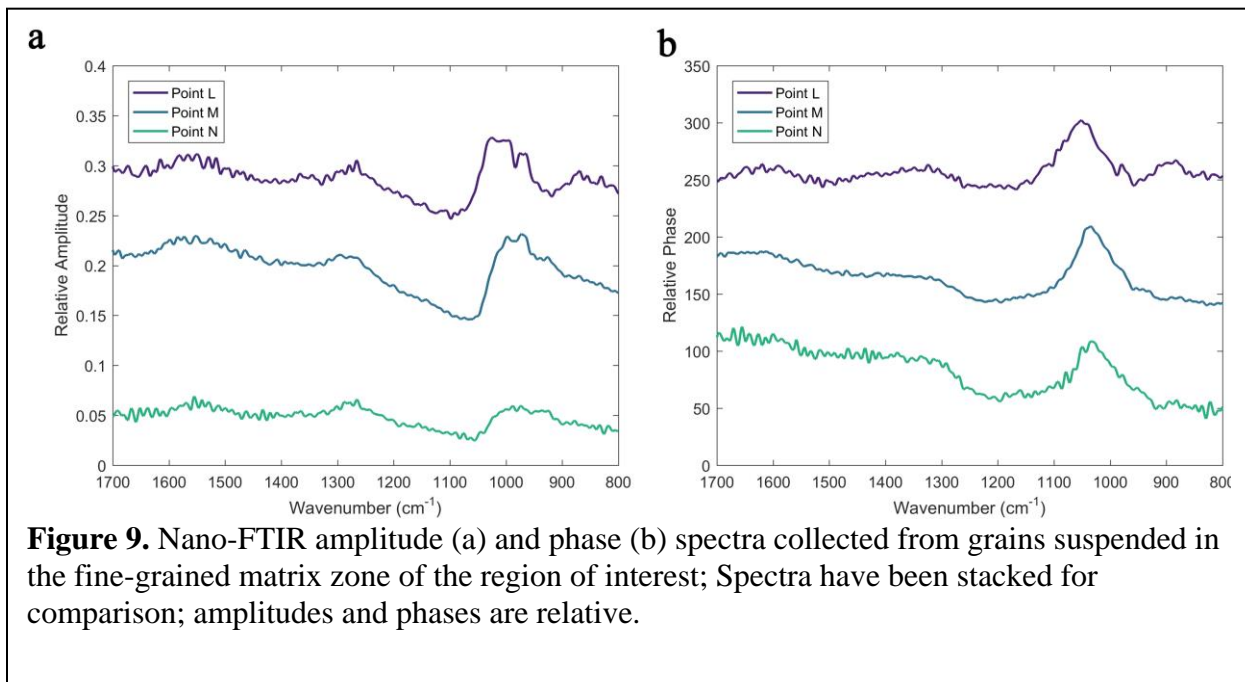
282 1082 and 1055 cm^{-1} respectively. As in the amplitude spectra, these broad bands have decreasing
 283 intensity as well, with spectrum E having the most intense peak.



284 We collected additional spectra, shown in Figure 8, from four positions in the outlying
 285 fine-grained matrix: H, I, J, and K. The amplitude spectrum of Point H has two amplitude maxima
 286 at 970 and 1020 cm^{-1} and a third broad maximum centered at $\sim 850 \text{ cm}^{-1}$. Spectrum K has a single
 287 broad maximum centered around 960 cm^{-1} , and spectrum J has the same feature with an overall
 288 higher amplitude. Spectrum I has a prominent amplitude maximum at 1030 cm^{-1} and a smaller
 289 feature at 970 cm^{-1} . The phase spectra of these points present a prominent and well-defined peak



290 near 1040 cm^{-1} . Spectra I and H additionally present a weaker band at 980 cm^{-1} , which is not
 291 resolved in spectra K and J.



292 Finally, three spectra were collected from positions on grains suspended in the fine-grained
 293 matrix: L, M, and N (Figure 9.). Amplitude spectrum L has amplitude maxima at 970 and 1020
 294 cm^{-1} . Spectrum M also has two maxima at 970 cm^{-1} , the other at 1000 cm^{-1} . Finally, spectrum N

295 is relatively flat, but has a broad maximum centered at 980 cm^{-1} . Their corresponding phase spectra
296 present a broad symmetric band centered around $1030\text{-}1050\text{ cm}^{-1}$. A smaller feature at 978 cm^{-1}
297 and a broad bump at 896 cm^{-1} are also present in spectrum L. We note that most of the spectra
298 presented here also have a broad feature near 1275 cm^{-1} .

299 **5. Discussion**

300 We place the point spectra collection positions, described in the results section, into two
301 main groups. The spectra collected from member positions of a given group share similar feature
302 positions and overall line shapes, in both their amplitude and phase spectra. This suggests that the
303 materials represented by the positions/point spectra of a group are compositionally similar. We
304 also define a third group containing points with flat and featureless spectra. Points E and N belong
305 to this group and are omitted from discussion.

306 The members of group 1 are spectra A, D and B. Spatially, points A and B exist on the
307 inner portion of the chondrule exposure, $\sim 1\text{-}1.5\text{ }\mu\text{m}$ from the chondrule-matrix boundary, while
308 point B is on the chondrule rim. The amplitude spectra of these points are dissimilar; spectra A
309 and B have sharp, well-defined reflectance features while spectrum D has weaker and broader
310 features. However, all three spots have spectral features at similar positions. Furthermore, when
311 we observe the phase spectra of each position the relationship becomes much clearer. Figure 10
312 shows a comparison of the amplitude and phase spectra of positions A, D, and B, as well as nano-
313 FTIR amplitude and phase spectra of single crystal enstatite (this study), forsterite (Dominguez et
314 al., 2014), and olivine chondrule spectra from Yesiltas et al. (2020). The phase spectra of points A
315 and D have prominent features around 925 , 960 , and 985 cm^{-1} , suggesting that the material these
316 spectra represent are compositionally similar. The difference in strength of observed features in

317 the amplitude spectra A and D are likely a result of local crystal orientation (Figure 11). These
 318 spectra match closely the nano-FTIR spectra of olivine in Didim (H3-5 chondrite) (Yesiltas et al.
 319 2020). The forsterite nano-FTIR amplitude spectrum of Dominguez et al. (2014) appears different
 320 than the amplitude spectra of points A, D, and B. While there are observable shifts in feature
 321 positions between the point spectra and the pure forsterite spectrum, the point spectra resemble the
 322 forsterite spectrum more closely than that of the pure enstatite spectrum. Furthermore, the
 323 amplitude spectra of points A, D, and B are also in disagreement with amplitude spectra
 324 (Dominguez et al., 2014) and emissivity spectra of pyroxenes (Hamilton, 2000). Therefore, we

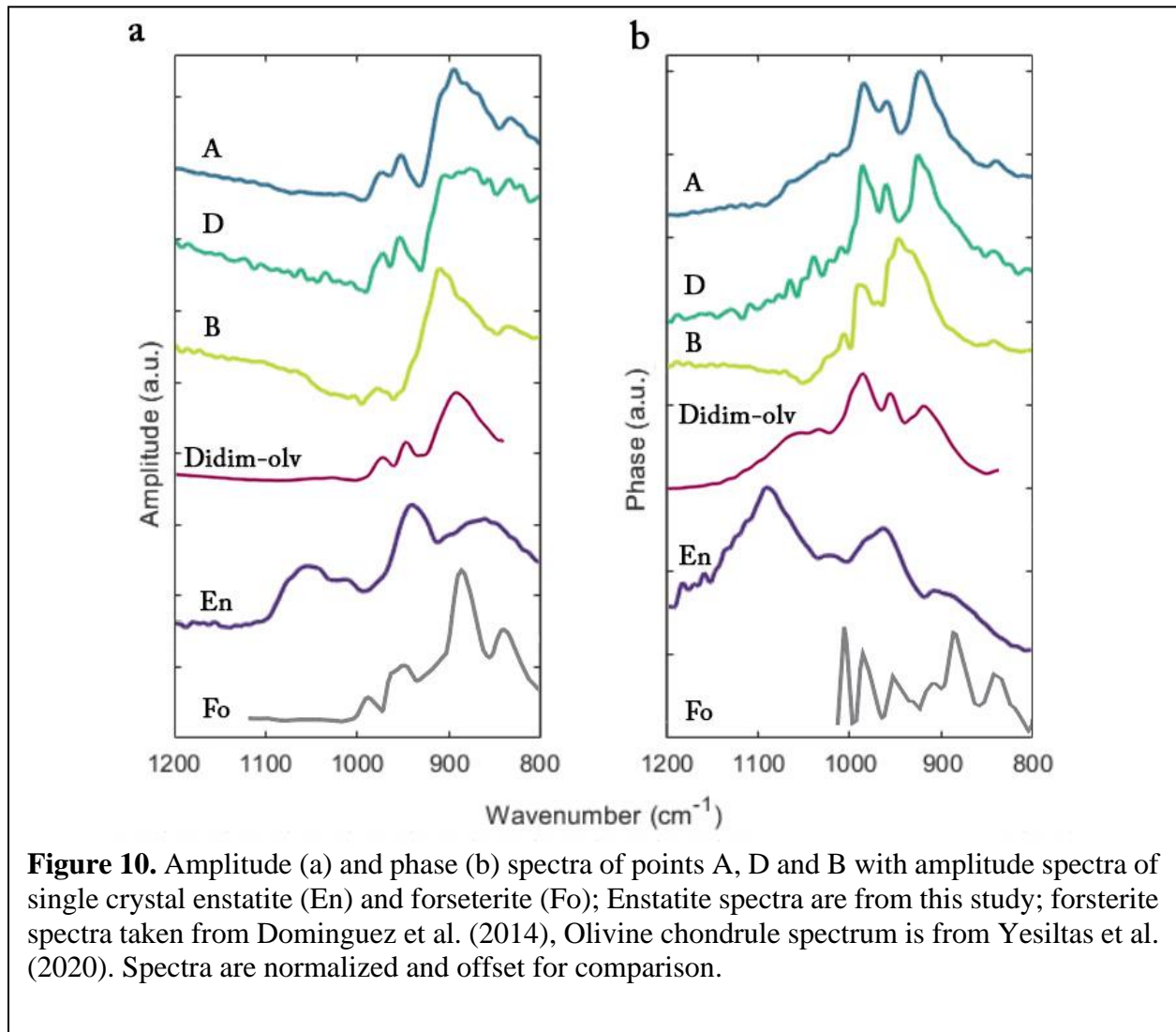


Figure 10. Amplitude (a) and phase (b) spectra of points A, D and B with amplitude spectra of single crystal enstatite (En) and forsterite (Fo); Enstatite spectra are from this study; forsterite spectra taken from Dominguez et al. (2014), Olivine chondrule spectrum is from Yesiltas et al. (2020). Spectra are normalized and offset for comparison.

325 interpret the spectra of A, D, and B as olivine with spectral differences resulting from variable
 326 crystal orientation.

327 In amplitude spectrum A, we attribute features at 895 cm^{-1} , 952 cm^{-1} , 974 cm^{-1} to the
 328 asymmetric Si-O stretch (ν_3) and the 832 cm^{-1} feature to the symmetric O-Si-O stretch (ν_1)
 329 (Reynard et al., 1991; Hamilton, 2010). While identifying olivine as the material observed at points
 330 A, D, and B is relatively straightforward, understanding exact forsterite-fayalite composition is
 331 less so. Chondrules in CM chondrites are observed to have Fe/Mg ratio values < 0.4 (Hezel &

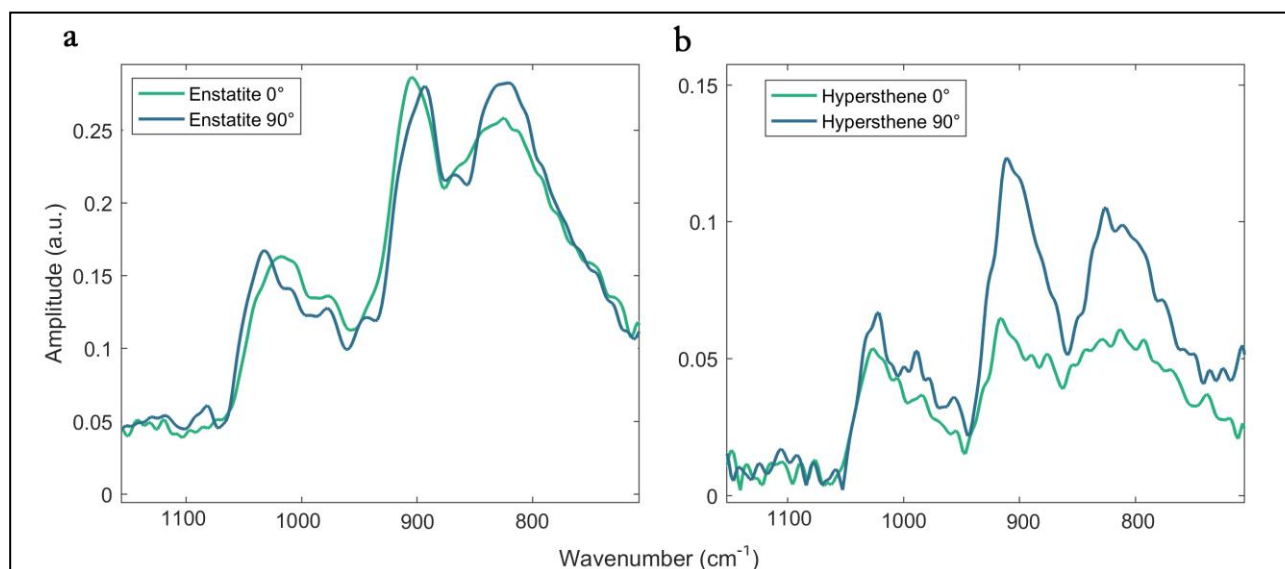


Figure 11. (a) Nano-FTIR amplitude spectra of single-crystal enstatite; These spectra were collected from the same crystallographic face (a-face) but offset by a 90° rotation. (b) Nano-FTIR amplitude spectra of a single-crystal hypersthene; These spectra were collected from the same crystallographic face (a-face) but offset by a 90° rotation; Both spectral pairs demonstrate that changing crystal orientation can cause shifts in band position and strength.

332 Palme, 2010; Palme et al., 2015; Friend et al., 2016), likely resulting from the high resistance of
 333 Mg-rich silicates to aqueous alteration (Zolensky et al., 1993). This suggests that the sample
 334 olivine is forsteritic in composition. However, chondrule rims and zones $4\text{--}15\ \mu\text{m}$ from the rims
 335 of chondrules once subjected to aqueous alteration processes have been observed to have
 336 significant Mg depletion compared to the chondrule core (Kereszturi et al., 2014; Kereszturi et al.,

337 2015). A large body of both experimental and modelling work investigating the MIR spectral
338 properties of the forsterite-fayallite olivine solid solution has been conducted (Duke & Stephens,
339 1964; Burns & Huggins, 1972; Dorschner et al., 1995; Fabian et al., 2001; Dyar et al., 2009;
340 Hamilton, 2010; Lane et al., 2011). Collectively, these works demonstrate that there is a
341 relationship between the peak positions of various MIR spectral bands and the ratio of Mg/Fe
342 cations that fill the olivine M1 and M2 sites.

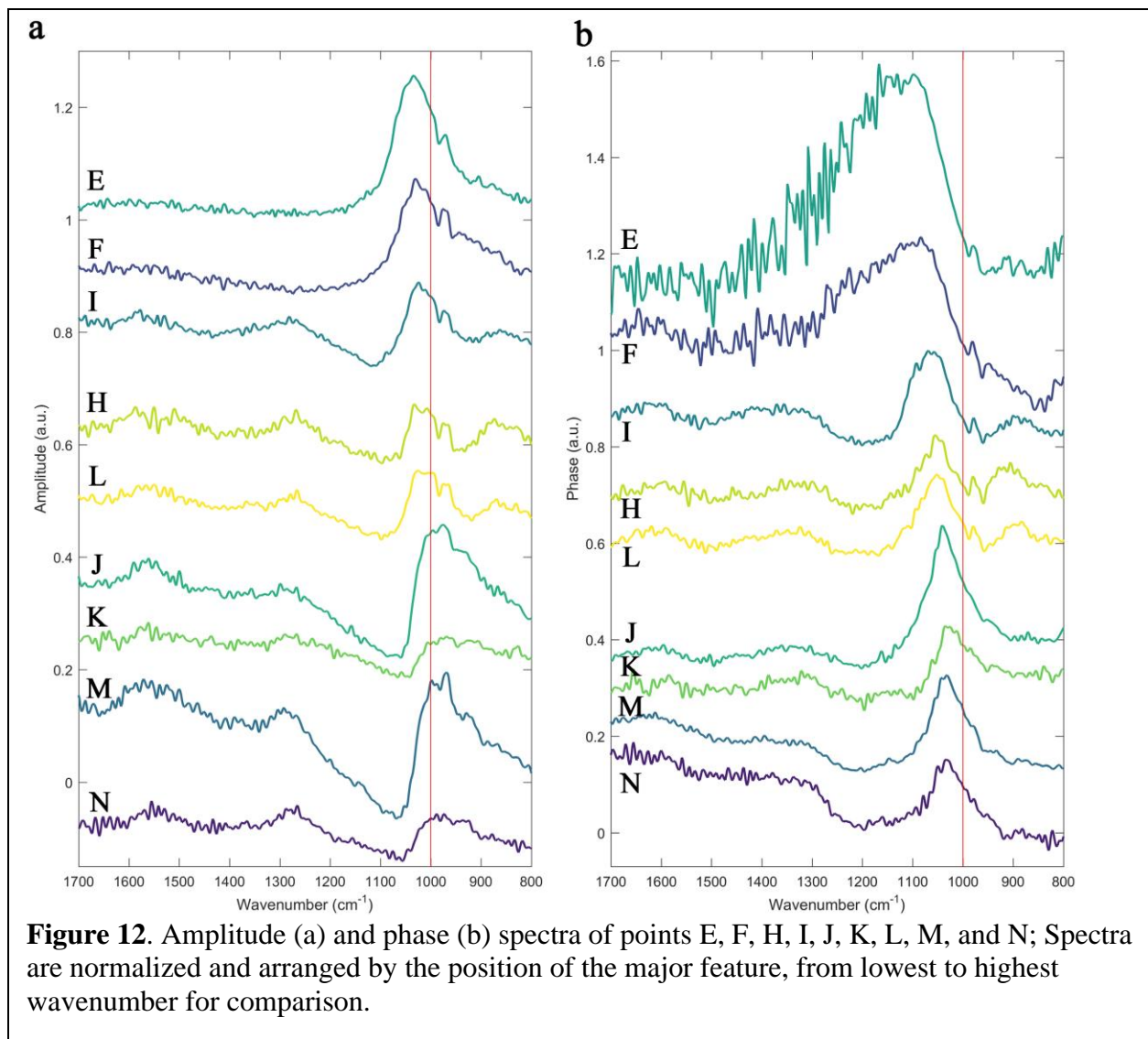
343 Lane et al. (2011), produced several, highly correlative ($R^2 \geq 0.9$) linear functions
344 describing the relationship between a spectral band's peak position and the forsterite content of an
345 olivine sample. Applying these functions on the amplitude spectra of points A and D would suggest
346 that the represented material is an $F_{070} - F_{090}$ olivine. It's clear from this body of literature that
347 the MIR behavior of olivine spectra also depends on the cationic impurity and crystallographic
348 orientation of a sample. Crystallite sizes of olivine may also effect the spectral band positions
349 (Hamilton et al. 2020). Indeed, comparison of the same spectra with Hamilton et al. (2020)
350 indicates relatively less forsteritic composition ($F_{035} - F_{060}$). Furthermore, the strong
351 electromagnetic coupling between the sample and the AFM tip distorts the vibrational modes of a
352 sample, resulting in shifts of band positions and changes in band shape. As a result, our
353 interpretation should be treated with caution.

354 Figure 11 shows two examples of the dependance of nano-FTIR spectra on crystallographic
355 orientation. This figure displays four spectra; two collected from a single enstatite crystal and two
356 collected from a single hypersthene crystal. In both cases the crystal was oriented, so the IR source
357 was normal to the crystallographic a-face but separated by a 90° rotation with respect to the normal
358 vector of the a-face. For both minerals, rotation by 90° leads to shifts in band position of the
359 mineral's MIR features. Changing the orientation of the crystal can also diminish the strength of a

360 given feature. The difference in strength of features in the two hypersthene spectra is similar to the
361 difference observed between the features of amplitude spectra A, D, and B. The crystal orientation
362 along with cation impurity and material form further obfuscate the role of Mg/Fe in the positions
363 of olivine nano-FTIR spectra. Further investigation into the relative importance of these variables
364 is required.

365 The other major position group, Group 2, has the most members: points L, H, K, J, E, I, M,
366 F, and N. Most of the points are in the fine-grain matrix or the suspended grains therein, but points
367 E and F are located in the bottom right corner zone of the chondrule exposure. While band feature
368 strength and exact position vary, each spectrum has a prominent amplitude maximum between
369 $\sim 990\text{-}1010\text{ cm}^{-1}$ and an ancillary feature $\sim 940\text{-}970\text{ cm}^{-1}$ (Figure 12a). The vertical red line at 1000
370 cm^{-1} clearly shows the spectral shift of the main silicate band from 990 to 1010 cm^{-1} . The phase
371 spectra are largely in agreement as well, with each spectrum having one main prominent feature
372 between $1040 - 1100\text{ cm}^{-1}$. A small feature at $\sim 970\text{ cm}^{-1}$ is also observed in some spectra. Based
373 on the general position of the main absorption feature in the observed phase spectra, the materials
374 that these points represent are likely hydrous phyllosilicate minerals. The main phyllosilicate band,
375 which is caused by Si – O stretching vibrations in the SiO_4 molecules composing the mineral's
376 tetrahedral sheet, occurs $\sim 1000\text{-}1100\text{ cm}^{-1}$ (Brindley & Zussman, 1959). This is a reasonable
377 assignment, as ALH 83100 has been observed to be composed of $\sim 85\%$ hydrous phyllosilicates
378 (Howard et al., 2011) and the observed amplitude spectra are consistent with reflectance spectra
379 of previous measurements of ALH 83100 (Lindgren et al., 2020). Furthermore, we have shown
380 the area surrounding the observed chondrule is rich in OH bearing material (Figure 1). The exact

381 phyllosilicate observed in each spectrum is debatable, however we limit possible phases to those
 382 readily observed in CM2 chondrites.



383 The Mg-rich serpentines (chrysotile, antigorite, lizardite) and Fe-cronstedtite are observed
 384 in both matrix and the rims of chondrules in CM2 chondrites (Zega & Buseck, 2003; Velbel &
 385 Palmer, 2011) and make up ~62 and ~20-24 vol % of ALH 83100 respectively (Howard et al.,
 386 2011; Lindgren et al., 2020). MIR spectra of cronstedtite and cronstedtite-rich mixtures are largely
 387 in disagreement with the spectra of points E, I, and F shown in Figure 12. (Bates et al., 2020;
 388 Breitenfeld et al., 2020). Using laboratory emissivity spectra and Kirchhoff's law ($R=1-E$), we

389 show that the amplitude spectra of points E, I, and F are in good agreement with the reflectance
 390 spectrum of antigorite (Breitenfeld et al., 2020) (Figure 13). In contrast, the amplitude spectra of
 391 points K, J, M and N are in poor agreement with the reflectance spectra of saponite and antigorite.
 392 However, amplitude spectra K, J, and N match up quite well with the reflectance spectrum of

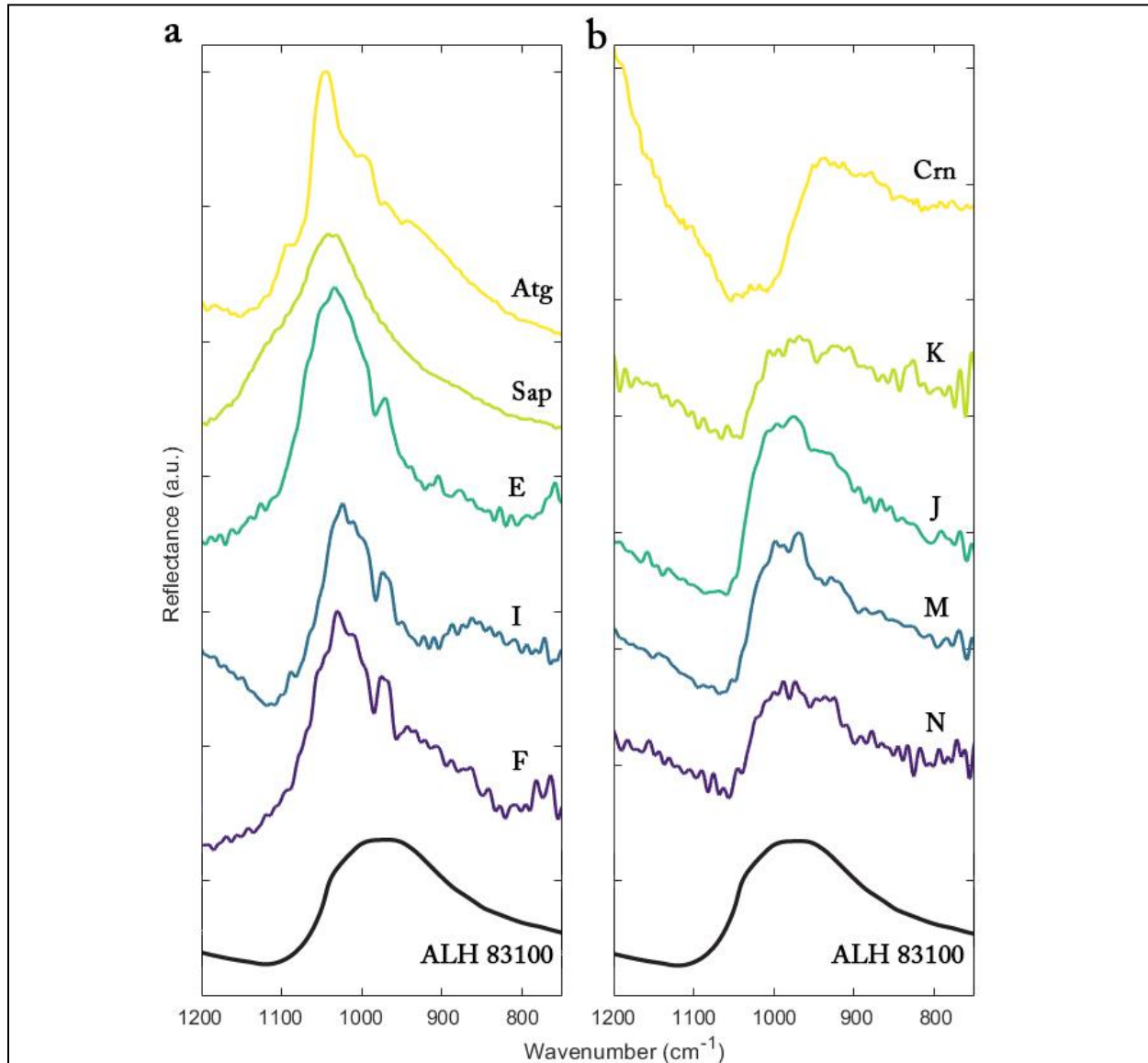


Figure 13. (a) Reflectance spectrum of pure antigorite and saponite pellets (Breitenfeld et al., 2020) and the amplitude spectra of points E, I, and F. (b) Reflectance spectrum of pure cronstedtite (Breitenfeld et al., 2021) and amplitude spectra of points K, J, M, and N; Spectrum ALH 83100 reproduced from (Lindgren et al., 2020). Spectra are normalized and offset for comparison.

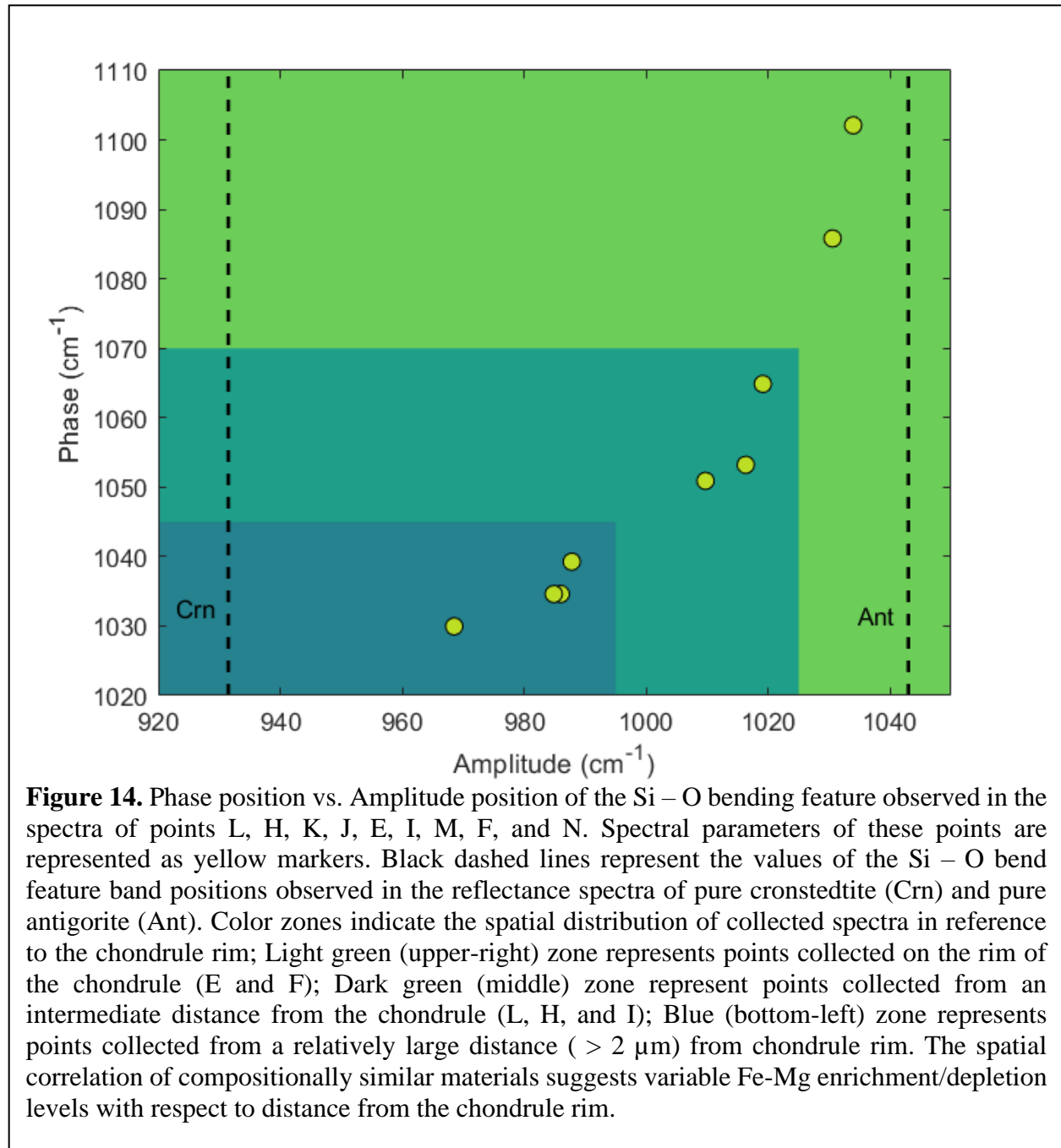
393 cronstedtite (Figure 13). Finally, reflectance spectra L and H do not have exact agreement with

394 either pure mineral phase. Rather, these spectra appear to be intermediates of the Fe and Mg rich
395 phyllosilicate phases.

396 The existence of multiple phyllosilicate phases is also supported by the observed variation
397 in band position and overall shape of these spectra. Phase spectra K, J, M, and N have Si-O bend
398 positions around 1029, 1039, 1034, and 1034 cm^{-1} respectively. In terms of amplitude, spectra K,
399 J, M, and N each have a prominent maximum centered around 968, 987, 986, and 984 cm^{-1} . Phase
400 spectra L, H, and I have their Si-O bend positions shifted to higher wavenumber (lower
401 wavelength) with positions ~ 1050.91 , 1052.22 , and 1064.87 cm^{-1} . These three spectra also are
402 observed to have an additional absorption feature at $\sim 900 \text{ cm}^{-1}$. Amplitude spectra L, H, and I also
403 have prominent reflectance features at 1009, 1016, and 1019 cm^{-1} , respectively. Finally, phase
404 spectra E and F have an Si-O bend feature shifted to even higher wavenumbers at ~ 1086 and 1102
405 cm^{-1} . The broad shape (full-width $\sim 300 \text{ cm}^{-1}$) of this feature in phase spectra E and F contrasts
406 with the relatively thin/sharp features observed in the other phase spectra of this group.

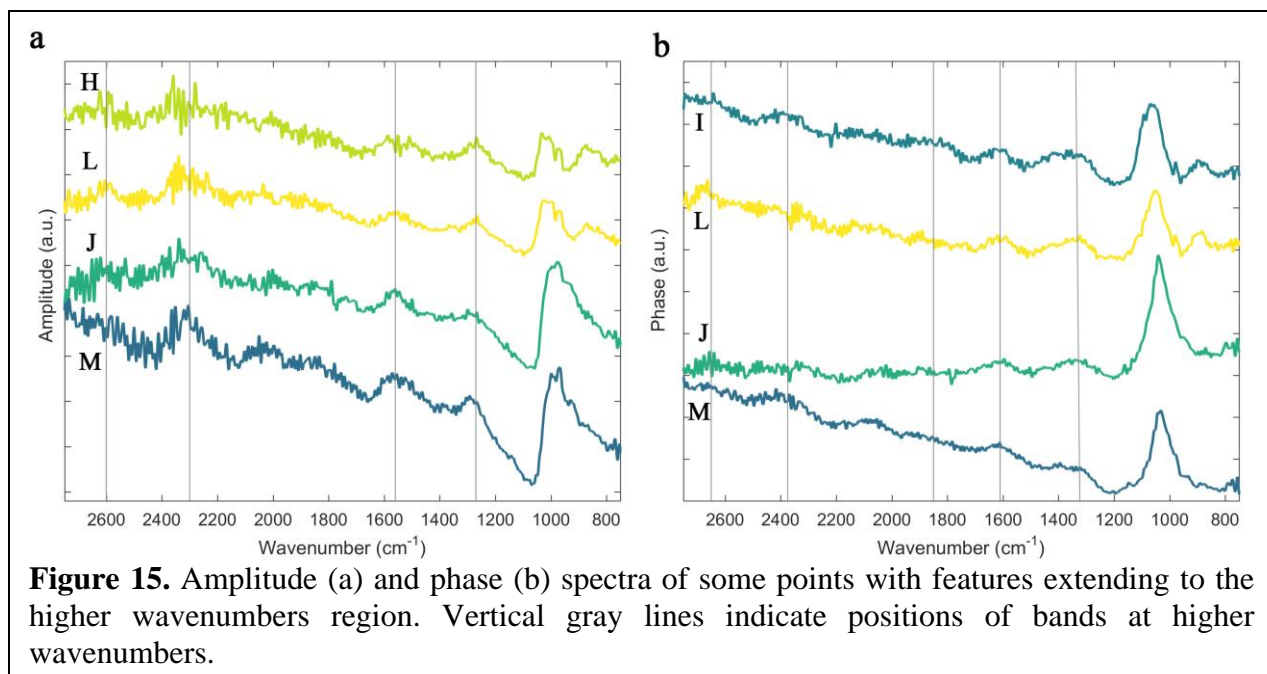
407 The spectral differences observed within this group of spectra are spatially distributed,
408 agreeing well with zones of optical amplitude variation observed in the $10.17 \mu\text{m}$ map displayed
409 in Figure 4. The position of the Si-O bend feature, in both amplitude and phase spectra, shifts to
410 shorter wavenumber as distance from the chondrule rim grows. The respective Si-O features of
411 spectra E and F have the highest wavenumber positions and were collected from the chondrule
412 rim. Spectra L, H, and I have intermediate wavenumber positions of their Si-O bending feature
413 and were collected from the zone of intermediate optical amplitude (orange colored matrix) of the
414 $10.17 \mu\text{m}$ map. Finally, spectra K, J, M, and N have the lowest wavenumber values of their Si-O
415 bending feature and were collected from the broad zone of high optical amplitude in the $10.17 \mu\text{m}$
416 map. We plot and compare the band position parameters of both phase and amplitude spectra in

417 Figure 14, which shows a strong polynomial-like correlation between the Si-O bending feature
 418 band positions observed in phase and amplitude spectra for a given point. We include the Si-O
 419 bending feature's band position from the reflectance spectrum of pure cronstedtite and antigorite,
 420 seen in Figure 15, to show that the spectra appear to exist on a continuum between the two pure
 421 mineral phases. We also show the spatial distribution of the points of interest as colored fields in



422 Figure 14. This figure shows that the points with spectra most in agreement with cronstedtite exist
 423 furthest from the chondrule rim and spectra most like antigorite exist close to or on the chondrule
 424 rim. As such, these data provide evidence for variable Fe-Mg enrichment/depletion zoning around
 425 the chondrule rim. Such evidence (Mg-rich/Fe-poor vs. Mg-poor/Fe-rich parts of the rim) suggests
 426 that aqueous alteration experienced by ALH 83100 may have occurred in the parent body as well
 427 as in the solar nebula as nebular alteration results in the mixing of different phyllosilicate
 428 components (Brearley and Geiger, 1991) as observed in some CO3 chondrites (Brearley, 1990,
 429 1991). Additional investigations of chondrule rims in this and other CI/CM meteorites need to be
 430 investigated to provide a better constraint on the origin of alteration for the rims.

431 All discussion thus far has considered spectral features within the wavenumber range of
 432 $\sim 800\text{-}1200\text{ cm}^{-1}$. The low wavenumber cutoff is due to the MCT detector used in this work.
 433 However, in higher wavenumber amplitude spectra, broad but well-defined features around 1250,
 434 1560, 2300, and 2600 cm^{-1} are observed (Figure 15). For phase spectra, features are seen around
 435 1340, 1600, 1850, and 2375, and 2650 cm^{-1} can be observed in certain spectra. However, it remains



436 unclear whether these features correspond to actual molecular vibrations or are artifacts introduced
437 by the nano-FTIR experimental setup.

438 An argument for these bands being artifacts rather than representing molecular vibrational
439 modes is that they appear consistently in the spectra of mineral phases we've identified as
440 structurally distinct (e.g., olivine vs. antigorite). They appear somewhat repetitive. However, this
441 is not the case for all points; the spectra of points E and F do not have these observed features.
442 Furthermore, the features seen at higher wavenumbers are not characteristic of silicate vibrational
443 modes. Rather the features seen in the 1250-3000 range are more likely the result of carbon bond
444 based absorptions. The C=C vibration (ν), a characteristic feature of insoluble organic matter
445 (IOM), has a corresponding absorption at $\sim 1600\text{ cm}^{-1}$ (Orthous-Daunay et al., 2013). Furthermore,
446 the CH₂ (δ_s) vibration has absorptions at 1300-1400 cm^{-1} (Fuente et al., 2003). As carbonaceous
447 molecules are a large component of carbonaceous chondrites, observed carbon absorption features
448 are not a surprising result.

449 While there is agreement between the high wavenumber features and carbon-based
450 absorptions, there are still issues with definitively assigning vibrational modes to the observed
451 features. These features occur with a periodicity; starting with the 1250 feature in amplitude
452 spectra, they continually occur $\sim 300\text{ cm}^{-1}$ apart consistently. The features appear oscillatory,
453 occurring as broad peaks with broad troughs separating them (Figure 15). Nano-FTIR has a depth
454 sensitivity of 50-100 nm and the observed features could potentially be due to the material within
455 the meteorite sample. This sinusoidal behavior is consistent with that of spectral interference
456 fringes, resulting from internal reflections within thin material films (Teolis et al., 2007; Azarfar
457 et al., 2018). While thin phyllosilicate layers could provide a structure for internal reflections to
458 occur, an alternative material to compose a possible thin film, in this sample, is IOM. The main

459 evidence that internal reflections, due to the thin platy structure, of a phyllosilicate ring are not at
460 play is that interference fringes are seen in the spectra of points representing both olivine and
461 phyllosilicates. These olivine points likely do not have overlying phyllosilicate materials but could
462 have thin overlying IOM films. The 1.9 wt.% C content of ALH 83100 (Alexander et al. 2013)
463 may account for such IOM thin films.

464 In summary, the sinusoidal features observed are likely not actual reflectance or absorption
465 features representing a specific carbon vibration. Rather they are the result of internal reflections
466 of light within IOM materials within the sample. This phenomenon makes identification of specific
467 organic functional groups and therefore specific carbonaceous molecules difficult if not
468 impossible. Ironically, this behavior is also currently the best evidence of carbonaceous molecules
469 in the sampled area of interest (via nano-FTIR).

470 **6 Conclusion**

471 We have presented nano-FTIR images and spectra of the carbonaceous chondrite ALH
472 83100. From the spectra, we have identified olivine, Mg-serpentine and cronstedtite. The focused
473 area includes a chondrule, its rim and the matrix. The spectra representing the chondrule indicates
474 a forsteritic composition (Fo₇₀₋₉₀), while the spectra of phyllosilicate minerals within the rim and
475 nearby matrix revealed that there is a spatial distribution of Fe-Mg enrichment/depletion
476 surrounding the chondrule rim. This suggests a heterogeneous aqueous alteration of the rim in the
477 parent body and hence the heterogeneous composition for the rim. Varying Fe-Mg distribution in

478 the rim might also indicate aqueous alteration for ALH 83100 in the parent body as well as in the
479 solar nebula.

480 This is the first study to apply multi-spectral IR imaging of a meteorite at the nano-scale.
481 In the context of meteoritics, nano-FTIR spectroscopy and imaging are still novel techniques.
482 Further quantitative analyses of this and other extraterrestrial samples will be enabled by the
483 creation of nano-FTIR mineral spectral libraries that account for crystal orientation and
484 development of methods to address interference fringe effects. Improvements to experimental
485 hardware, such as the introduction of multi-wavelength light sources for spectral imaging will do
486 the same. Nanoscale investigations of the characteristic features of primitive carbonaceous
487 chondrites, especially those like ALH 83100 that is an intermediate between CM1/2 and contains
488 signatures of varying degrees of aqueous alteration, can potentially allow us to better constrain the
489 nebular as well as parent body processes.

490 **Acknowledgments**

491 This work was supported by the RIS⁴E and RISE2 nodes (T. D. Glotch, PI) of NASA's Solar
492 System Exploration Research Virtual Institute. This research used resources of the Advanced Light
493 Source, a U.S. DOE Office of Science User Facility under contract no. DE-AC02-05CH11231.
494 MY acknowledges support from TUBITAK (projects 119N207 and 120Y115). U.S. Antarctic
495 meteorite samples are recovered by the Antarctic Search for Meteorites (ANSMET) program that
496 has been funded by NSF and NASA, and characterized and curated by the Department of Mineral
497 Sciences of the Smithsonian Institution and Astromaterials Curation Office at NASA Johnson
498 Space Center.

499 **Data Availability Statement**

500 The data collected and used by this work will be stored in a repository at Zenodo.org upon
501 acceptance of the manuscript and will be found by searching for the DOI assigned to this work.
502 Nano-IR spectra are provided for the reviewers as an Excel spreadsheet in Supplementary
503 Information.

504 **References**

- 505 Alexander, C.M.O.D., Fogel, M., Yabuta, H. and Cody, G.D., 2007. The origin and evolution of
506 chondrites recorded in the elemental and isotopic compositions of their macromolecular
507 organic matter. *Geochimica et Cosmochimica Acta*, 71(17), 4380-4403.
- 508 Alexander, C.M.D., Howard, K.T., Bowden, R. and Fogel, M.L., 2013. The classification of CM
509 and CR chondrites using bulk H, C and N abundances and isotopic compositions. *Geochimica
510 et Cosmochimica Acta*, 123, pp.244-260.
- 511 Amarie, S., Ganz, T. and Keilmann, F. (2009), Mid-infrared near-field spectroscopy. *Optics
512 Express*, 17(24), 21794-21801.
- 513 Amenabar, I., Poly, S., Nuansing, W., Hubrich, E.H., Govyadinov, A.A., Huth, F., Krutokhvostov,
514 R., Zhang, L., Knez, M., Heberle, J. and Bittner, A.M. (2013), Structural analysis and mapping
515 of individual protein complexes by infrared nanospectroscopy. *Nature Communications*, 4(1),
516 1-9.
- 517 Azarfar, G., Aboualizadeh, E., Walter, N.M., Ratti, S., Olivieri, C., Norici, A., Nasse, M., Kohler,
518 A., Giordano, M. and Hirschmugl, C.J. (2018), Estimating and correcting interference fringes
519 in infrared spectra in infrared hyperspectral imaging. *Analyst*, 143(19), 4674-4683.
- 520 Bates, H. C., A. J. King, K. L. Donaldson Hanna, N. E. Bowles, and S. S. Russell. (2020), "Linking
521 mineralogy and spectroscopy of highly aqueously altered CM and CI carbonaceous chondrites
522 in preparation for primitive asteroid sample return." *Meteoritics & Planetary Science*, 55(1)
523 77-101.
- 524 Bechtel, H. A., Johnson, S. C., Khatib, O., Muller, E. A., & Raschke, M. B. (2020), Synchrotron
525 infrared nano-spectroscopy and-imaging. *Surface Science Reports*, 75(3), 100493.
- 526 Brearley, A.J., 1990, March. Matrix Mineralogy of the Unequilibrated CO3 Chondrite, ALH
527 A77307: Evidence for Disequilibrium Condensation Processes and Implications for the Origin
528 of Chondrite Matrices. In Lunar and Planetary Science Conference, 21,125.
- 529 Brearley, A.J., 1991, March. Subsolidus microstructures and cooling history of pyroxenes in the
530 Zagami shergottite. In Lunar and Planetary Science Conference, 22, 133.
- 531 Brearley, A.J. and Geiger, T., 1991. Mineralogical and chemical studies bearing on the origin of
532 accretionary rims in the Murchison CM2 carbonaceous chondrite. *Meteoritics*, 26, p.323.
- 533 Breitenfeld, L. B., A. D. Rogers, T. D. Glotch, V. E. Hamilton, P. R. Christensen, D. S. Lauretta,
534 M. E. Gemma, K. T. Howard, D. S. Ebel, G. Kim, A. M. Kling, H. Nekvasil, and N. J.
535 DiFrancesco (2021), Machine learning mid-infrared spectral models for predicting modal
536 mineralogy of CI/CM chondritic asteroids and Bennu, *J. Geophys. Res.*, 126, e2021JE007035,
537 doi:10.1029/2021JE007035.
- 538 Brindley, G. W., J. Zussman. (1959), Infra-red absorption data for serpentine minerals. *American
539 Mineralogist* 44(1-2): 185–188.
- 540 Burns, R.G. and Huggins, F.E.(1972), Cation determinative curves for Mg-Fe-Mn olivines from
541 vibrational spectra. *American Mineralogist: Journal of Earth and Planetary Materials*, 57(5-
542 6), 967-985.

- 543 Clark, R.N. and Roush, T.L. (1984), Reflectance spectroscopy: Quantitative analysis techniques
544 for remote sensing applications. *Journal of Geophysical Research: Solid Earth*, 89(B7), 6329-
545 6340.
- 546 De Leuw, S., Rubin, A.E., Schmitt, A.K. and Wasson, J.T. (2009), *Mn-Cr Systematics for the*
547 *CM2. 1 Chondrites QUE 93005 and ALH 83100: Implications for the Timing of Aqueous*
548 *Alteration*. Paper presented at 40th Lunar and Planetary Science Conference, Houston, Texas
- 549 de LEUW, S., Rubin, A.E. and Wasson, J.T., 2010. Carbonates in CM chondrites: Complex
550 formational histories and comparison to carbonates in CI chondrites. *Meteoritics & Planetary*
551 *Science*, 45(4), pp.513-530.
- 552 Dominguez, G., Mcleod, A.S., Gainsforth, Z., Kelly, P., Bechtel, H.A., Keilmann, F., Westphal,
553 A., Thiemens, M. and Basov, D.N. (2014), Nanoscale infrared spectroscopy as a non-
554 destructive probe of extraterrestrial samples. *Nature Communications*, 5(1), 1-10.
- 555 Dorschner, J., Begemann, B., Henning, T., Jaeger, C. and Mutschke, H. (1995), Steps toward
556 interstellar silicate mineralogy. II. Study of Mg-Fe-silicate glasses of variable
557 composition. *Astronomy and Astrophysics*, 300, 503.
- 558 Duke, D.A. and Stephens, J.D. (1964), Infrared investigation of the olivine group minerals.
559 *American Mineralogist: Journal of Earth and Planetary Materials*, 49(9-10), 1388-1406.
- 560 Dürig, U., Pohl, D.W. and Rohner, F. (1986), Near-field optical-scanning microscopy. *Journal of*
561 *Applied Physics*, 59(10), 3318-3327.
- 562 Dyar, M.D., Sklute, E.C., Menzies, O.N., Bland, P.A., Lindsley, D., Glotch, T., Lane, M.D.,
563 Schaefer, M.W., Wopenka, B., Klima, R. and Bishop, J.L. (2009), Spectroscopic
564 characteristics of synthetic olivine: An integrated multi-wavelength and multi-technique
565 approach. *American Mineralogist*, 94(7), 883-898.
- 566 Elsila, J.E., Charnley, S.B., Burton, A.S., Glavin, D.P. and Dworkin, J.P. (2012), Compound-
567 specific carbon, nitrogen, and hydrogen isotopic ratios for amino acids in CM and CR
568 chondrites and their use in evaluating potential formation pathways. *Meteoritics & Planetary*
569 *Science*, 47(9), 1517-1536.
- 570 Fabian, D., Henning, T., Jäger, C., Mutschke, H., Dorschner, J. and Wehrhan, O. (2001), Steps
571 toward interstellar silicate mineralogy-VI. Dependence of crystalline olivine IR spectra on iron
572 content and particle shape. *Astronomy & Astrophysics*, 378(1), 228-238.
- 573 Farrand, W.H., Wright, S.P., Rogers, A.D. and Glotch, T.D. (2016), Basaltic glass formed from
574 hydrovolcanism and impact processes: Characterization and clues for detection of mode of
575 origin from VNIR through MWIR reflectance and emission spectroscopy. *Icarus*, 275, 16-28.
- 576 Farrand, W.H., Wright, S.P., Glotch, T.D., Schröder, C., Sklute, E.C. and Dyar, M.D., 2018.
577 Spectroscopic examinations of hydro- and glaciovolcanic basaltic tuffs: Modes of alteration
578 and relevance for Mars. *Icarus*, 309, 241-259.
- 579 Friedlander, L.R., Glotch, T.D., Bish, D.L., Dyar, M.D., Sharp, T.G., Sklute, E.C. and Michalski,
580 J.R. (2015), Structural and spectroscopic changes to natural nontronite induced by
581 experimental impacts between 10 and 40 GPa. *Journal of Geophysical Research:*
582 *Planets*, 120(5), 888-912.

- 583 Friend, P., Hezel, D.C., Barrat, J.A., Zipfel, J. and Palme, H. (2016), *The Chemical Composition*
584 *of Matrix, Chondrules and Bulk Meteorite of the CM Chondrite Jbilet Winselwan*. Paper
585 presented at the 47th Lunar and Planetary Science Conference.
- 586 Fuente, E., Menéndez, J.A., Díez, M.A., Suárez, D. and Montes-Morán, M.A. (2003), Infrared
587 spectroscopy of carbon materials: a quantum chemical study of model compounds. *The Journal*
588 *of physical chemistry B*, 107(26), 6350-6359.
- 589 Gillespie, A. R., A. B. Kahle, and R. E. Walker (1986), Color enhancement of highly correlated
590 images. 1. Decorrelation and His contrast stretches, *Remote Sens. Environ.*, 20(3), 209–235,
591 doi:10.1016/0034-4257(86)90044-1.
- 592 Glotch, T.D., Young, J.M., Yao, Z., Bechtel, H.A., Hamilton, V.E., Christensen, P.R. and Lauretta,
593 D.S., 2019. Near-Field Infrared Spectroscopy as a Tool for Analysis of Chondritic Returned
594 Samples. LPI Contributions, 2189, p.2061.
- 595 Hamilton, V.E. (2000), Thermal infrared emission spectroscopy of the pyroxene mineral
596 series. *Journal of Geophysical Research: Planets*, 105(E4), 9701-9716.
- 597 Hamilton, V.E. (2010), Thermal infrared (vibrational) spectroscopy of Mg–Fe olivines: A review
598 and applications to determining the composition of planetary surfaces. *Geochemistry*, 70(1),
599 7-33.
- 600 Hamilton, V.E., Simon, A.A., Christensen, P.R., Reuter, D.C., Clark, B.E., Barucci, M.A., Bowles,
601 N.E., Boynton, W.V., Brucato, J.R., Cloutis, E.A. and Connolly, H.C. (2019), Evidence for
602 widespread hydrated minerals on asteroid (101955) Benu. *Nature Astronomy*, 3(4), 332-340.
- 603 Hamilton, V.E., Haberle, C.W. and Mayerhöfer, T.G., 2020. Effects of small crystallite size on the
604 thermal infrared (vibrational) spectra of minerals. *American Mineralogist: Journal of Earth and*
605 *Planetary Materials*, 105(11), pp.1756-1760.
- 606 Hamilton, V.E., Christensen, P.R., Kaplan, H.H., Haberle, C.W., Rogers, A.D., Glotch, T.D.,
607 Breitenfeld, L.B., Goodrich, C.A., Schrader, D.L., McCoy, T.J. and Lantz, C., 2021. Evidence
608 for limited compositional and particle size variation on asteroid (101955) Benu from thermal
609 infrared spectroscopy. *Astronomy & Astrophysics*, 650, p.A120.
- 610 Donaldson Hanna, K., Schrader, D.L., Cloutis, E.A., Cody, G.D., King, A.J., McCoy, T.J., Applin,
611 D.M., Mann, J.P., Bowles, N.E., Brucato, J.R. Connolly Jr, H.C., Dotto, E., Keller, L.P., Lim,
612 L.F., Clark, B.E., Hamilton, V.E., Lantz, C., Lauretta, D.S., Russell, S.S., and Schofield, P.F.
613 (2019). Spectral characterization of analog samples in anticipation of OSIRIS-REx's arrival at
614 Benu: A blind test study. *Icarus*, 319, pp.701-723.
- 615 Hapke, B. (1981), Bidirectional reflectance spectroscopy: 1. Theory. *Journal of Geophysical*
616 *Research: Solid Earth*, 86(B4), 3039-3054.
- 617 Hillenbrand, R. and Keilmann, F. (2000), Complex optical constants on a subwavelength
618 scale. *Physical Review Letters*, 85(14), 3029.
- 619 Howard, K.T., Benedix, G.K., Bland, P.A. and Cressey, G. (2011), Modal mineralogy of CM
620 chondrites by X-ray diffraction (PSD-XRD): Part 2. Degree, nature and settings of aqueous
621 alteration. *Geochimica et Cosmochimica Acta*, 75(10), 2735-2751.
- 622 Hunt, G.R. and Salisbury, J.W. (1970), Visible and near infrared spectra of minerals and rocks. I.
623 Silicates. *Modern Geology*, 2, 23-30.

- 624 Jaret, S.J., Woerner, W.R., Phillips, B.L., Ehm, L., Nekvasil, H., Wright, S.P. and Glotch, T.D.
625 (2015), Maskelynite formation via solid-state transformation: Evidence of infrared and X-ray
626 anisotropy. *Journal of Geophysical Research: Planets*, 120(3), 570-587.
- 627 Jaret, S.J., Johnson, J.R., Sims, M., DiFrancesco, N. and Glotch, T.D. (2018). Microspectroscopic
628 and petrographic comparison of experimentally shocked albite, andesine, and
629 bytownite. *Journal of Geophysical Research: Planets*, 123(7), pp.1701-1722.
- 630 Johnson, P.E., Smith, M.O., Taylor-George, S. and Adams, J.B. (1983), A semiempirical method
631 for analysis of the reflectance spectra of binary mineral mixtures. *Journal of Geophysical*
632 *Research: Solid Earth*, 88(B4), 3557-3561.
- 633 Johnson, J.R., Jaret, S.J., Glotch, T.D. and Sims, M., 2020. Raman and infrared microspectroscopy
634 of experimentally shocked basalts. *Journal of Geophysical Research: Planets*, 125(2),
- 635 Kaplan, H.H., Lauretta, D.S., Simon, A.A., Hamilton, V.E., DellaGiustina, D.N., Golish, D.R.,
636 Reuter, D.C., Bennett, C.A., Burke, K.N., Campins, H. and Connolly, H.C., 2020. Bright
637 carbonate veins on asteroid (101955) Bennu: Implications for aqueous alteration
638 history. *Science*, 370(6517)
- 639 Kebukawa, Y., Kobayashi, H., Urayama, N., Baden, N., Kondo, M., Zolensky, M.E. and
640 Kobayashi, K. (2019), Nanoscale infrared imaging analysis of carbonaceous chondrites to
641 understand organic-mineral interactions during aqueous alteration. *Proceedings of the*
642 *National Academy of Sciences*, 116(3), 753-758.
- 643 Kereszturi, A., Blumberger, Z., Józsa, S., May, Z., Müller, A., Szabó, M. and Tóth, M. (2014).
644 Alteration processes in the CV chondrite parent body based on analysis of NWA 2086
645 meteorite. *Meteoritics & Planetary Science*, 49(8), 1350-1364.
- 646 Kereszturi, A., Gyollai, I. and Szabó, M., (2015). Case study of chondrule alteration with IR
647 spectroscopy in NWA 2086 CV3 meteorite. *Planetary and Space Science*, 106, 122-131.
- 648 King, T.V. and Ridley, W.I. (1987), Relation of the spectroscopic reflectance of olivine to mineral
649 chemistry and some remote sensing implications. *Journal of Geophysical Research: Solid*
650 *Earth*, 92(B11), 11457-11469.
- 651 King, A.J., Solomon, J.R., Schofield, P.F. and Russell, S.S. (2015) Characterising the CI and CI-
652 like carbonaceous chondrites using thermogravimetric analysis and infrared spectroscopy.
653 *Earth, Planets and Space*, 67(1), 1-12.
- 654 Kitazato, K., Milliken, R.E., Iwata, T., Abe, M., Ohtake, M., Matsuura, S., Arai, T., Nakauchi, Y.,
655 Nakamura, T., Matsuoka, M. and Senshu, H. (2019), The surface composition of asteroid
656 162173 Ryugu from Hayabusa2 near-infrared spectroscopy. *Science*, 364(6437), 272-275.
- 657 Labardi, M., Patane, S. and Allegrini, M. (2000), Artifact-free near-field optical imaging by
658 apertureless microscopy. *Applied Physics Letters*, 77(5), 621-623.
- 659 Lane, M.D., T.D. Glotch, M.D. Dyar, C.M. Pieters, R. Klima, T. Hiroi, J.L. Bishop, and J.
660 Sunshine. (2011), "Midinfrared spectroscopy of synthetic olivines: Thermal emission, specular
661 and diffuse reflectance, and attenuated total reflectance studies of forsterite to
662 fayalite." *Journal of Geophysical Research: Planets* 116(E8)

- 663 Laurretta, D.S., DellaGiustina, D.N., Bennett, C.A., Golish, D.R., Becker, K.J., Balram-Knutson,
664 S.S., Barnouin, O.S., Becker, T.L., Bottke, W.F., Boynton, W.V. and Campins, H. (2019), The
665 unexpected surface of asteroid (101955) Bennu. *Nature*, 568(7750), 55-60.
- 666 Lindgren, P., Lee, M.R., Sparkes, R., Greenwood, R.C., Hanna, R.D., Franchi, I.A., King, A.J.,
667 Floyd, C., Martin, P.E., Hamilton, V.E. and Haberle, C. (2020), Signatures of the post-
668 hydration heating of highly aqueously altered CM carbonaceous chondrites and implications
669 for interpreting asteroid sample returns. *Geochimica et Cosmochimica Acta*, 289, 69-92.
- 670 Mayerhöfer, T.G., Pahlow, S., Hübner, U. and Popp, J. (2018), Removing interference-based
671 effects from the infrared transmittance spectra of thin films on metallic substrates: a fast and
672 wave optics conform solution. *Analyst*, 143(13), 3164-3175.
- 673 Mustard, J.F. and Pieters, C.M. (1987), Quantitative abundance estimates from bidirectional
674 reflectance measurements. *Journal of Geophysical Research: Solid Earth*, 92(B4), 617-626.
- 675 Nasse, M.J., Walsh, M.J., Mattson, E.C., Reininger, R., Kajdacsy-Balla, A., Macias, V., Bhargava,
676 R. and Hirschmugl, C.J., 2011. High-resolution Fourier-transform infrared chemical imaging
677 with multiple synchrotron beams. *Nature methods*, 8(5), pp.413-416.
- 678 Orthous-Daunay, F.R., Quirico, E., Beck, P., Brissaud, O., Dartois, E., Pino, T. and Schmitt, B.
679 (2013), Mid-infrared study of the molecular structure variability of insoluble organic matter
680 from primitive chondrites. *Icarus*, 223(1), 534-543.
- 681 Palme, H., Hezel, D. C., & Ebel, D. S. (2015). The origin of chondrules: Constraints from matrix
682 composition and matrix-chondrule complementarity. *Earth and Planetary Science
683 Letters*, 411, 11-19.
- 684 Pearson, V.K., Sephton, M.A., Kearsley, A.T., Bland, P.A., Franchi, I.A. and Gilmour, I. (2002),
685 Clay mineral-organic matter relationships in the early solar system. *Meteoritics & Planetary
686 Science*, 37(12), 1829-1833.
- 687 Reynard, B. (1991), Single-crystal infrared reflectivity of pure Mg₂SiO₂ forsterite and (Mg_{0.86}, Fe
688 _{0.14})₂SiO₄ olivine. *Physics and Chemistry of Minerals*, 18(1), 19-25.
- 689 Shirley, K.A. and Glotch, T.D. (2019), Particle size effects on mid-infrared spectra of lunar analog
690 minerals in a simulated lunar environment. *Journal of Geophysical Research: Planets*, 124(4),
691 970-988.
- 692 Simon, A.A., Kaplan, H.H., Hamilton, V.E., Laurretta, D.S., Campins, H., Emery, J.P., Barucci,
693 M.A., DellaGiustina, D.N., Reuter, D.C., Sandford, S.A. and Golish, D.R. (2020), Widespread
694 carbon-bearing materials on near-Earth asteroid (101955) Bennu. *Science*, 370(6517).
- 695 Takir, D., Emery, J.P., Mcsween Jr, H.Y., Hibbitts, C.A., Clark, R.N., Pearson, N. and Wang, A.
696 (2013), Nature and degree of aqueous alteration in CM and CI carbonaceous
697 chondrites. *Meteoritics & Planetary Science*, 48(9), 1618-1637.
- 698 Teolis, B.D., Loeffler, M.J., Raut, U., Famá, M. and Baragiola, R.A. (2007), Infrared reflectance
699 spectroscopy on thin films: Interference effects. *Icarus*, 190(1), 274-279.
- 700 Velbel, M.A. and Palmer, E.E. (2011), Fine-grained serpentine in CM2 carbonaceous chondrites
701 and its implications for the extent of aqueous alteration on the parent body: A review. *Clays
702 and Clay Minerals*, 59(4), 416-432.

- 703 Xu, X.G., Rang, M., Craig, I.M. and Raschke, M.B. (2012), Pushing the sample-size limit of
704 infrared vibrational nanospectroscopy: from monolayer toward single molecule
705 sensitivity. *The Journal of Physical Chemistry Letters*, 3(13), 1836-1841.
- 706 Yesiltas, M., Hirschmugl, C.J. and Peale, R.E., 2013. In situ investigation of meteoritic organic-
707 mineral relationships by high spatial resolution infrared spectroscopy. *Meteoritics and*
708 *Planetary Science Supplement*, 76, p.5068.
- 709 Yesiltas, M. and Kebukawa, Y. (2016), Associations of organic matter with minerals in Tagish
710 Lake meteorite via high spatial resolution synchrotron-based FTIR microspectroscopy.
711 *Meteoritics & Planetary Science*, 51(3), 584-595.
- 712 Yesiltas, M., Sedlmair, J., Peale, R.E. and Hirschmugl, C.J., 2017. Synchrotron-based three-
713 dimensional Fourier-transform infrared spectro-microtomography of Murchison meteorite
714 grain. *Applied spectroscopy*, 71(6), pp.1198-1208.
- 715 Yesiltas, M., Kaya, M., Glotch, T.D., Brunetto, R., Maturilli, A., Helbert, J. and Ozel, M.E. (2020),
716 Biconical reflectance, micro-Raman, and nano-FTIR spectroscopy of the Didim (H3-5)
717 meteorite: Chemical content and molecular variations. *Meteoritics & Planetary*
718 *Science*, 55(11), 2404-2421.
- 719 Yesiltas, M., T. D. Glotch, and B. Sava (2021), Nano-FTIR spectroscopic identification of
720 prebiotic carbonyl compounds in Dominion Range 08006 carbonaceous chondrite, *Scientific*
721 *Reports*, 11, 11656, doi:10.1038/s41598-021-91200-8.
- 722 Zega, T.J. and Buseck, P.R. (2003), Fine-grained-rim mineralogy of the Cold Bokkeveld CM
723 chondrite. *Geochimica et Cosmochimica Acta*, 67(9), 1711-1721
- 724 Zega, T.J., Garvie, L.A., Dódonny, I., Friedrich, H., Stroud, R.M. and Buseck, P.R. (2006),
725 Polyhedral serpentine grains in CM chondrites. *Meteoritics & Planetary Science*, 41(5), 681-
726 688.
- 727 Zolensky, M., Barrett, R. and Browning, L. (1993), Mineralogy and composition of matrix and
728 chondrule rims in carbonaceous chondrites. *Geochimica et Cosmochimica Acta*, 57(13), 3123-
729 3148.
- 730 Zolensky, M.E., Mittlefehldt, D.W., Lipschutz, M.E., Wang, M.S., Clayton, R.N., Mayeda, T.K.,
731 Grady, M.M., Pillinger, C. and David, B., 1997. CM chondrites exhibit the complete petrologic
732 range from type 2 to 1. *Geochimica et Cosmochimica Acta*, 61(23), pp.5099-5115.
733